Theoretical and experimental analysis of a horizontal planar Liquid-Vapour Thermal Diode (PLVTD)

Theoretical and experimental analysis of a horizontal Planar Liquid-Vapour Thermal Diode (PLVTD)

Adrian Pugsley (a.pugsley@ulster.ac.uk, +44(0)28 90366264 (corresponding author)
Aggelos Zacharopoulos (a.zacharopoulos@ulster.ac.uk) +44(0)28 90368227
Jayanta Deb Mondol (jd.mondol@ulster.ac.uk) +44(0)28 90368037
Mervyn Smyth (m.smyth1@ulster.ac.uk) +44(0)28 90368119

Centre for Sustainable Technologies (www.cst.ulster.ac.uk), School of the Built Environment, Ulster University, Newtownabbey, BT37 0QB, Northern Ireland, UK

Keywords

Thermal diode; one-way heat flow; phase change; solar collector; heat rejection

Highlights

- Horizontal planar unidirectional heat transfer device was realised (0.15m^2 PLVTD)
- Applications in solar collectors and climate control building envelopes
- One-dimensional lumped parameter heat transfer model developed & interrogated
- Forward mode heat transfer $150<U_f<500$ W·m^{-2}K^{-1} depends on temperature & heat flux
- Reverse mode insulation $U_r=2$ W·m^{-2}K^{-1} achievable using 70mm cavity for 97% diodicity

Abstract

Thermal diodes are unidirectional heat transfer devices, analogous to electrical diodes, which offer low resistance (thermal conductance) in one direction and high resistance (thermal insulation) in the other. Thermal diodicity has significant potential to improve the efficacy of a wide variety of heating and cooling devices. This paper presents pioneering work to experimentally measure the heat transfer characteristics of a 0.15m^2 passive Planar Liquid-Vapour Thermal Diode (PLVTD). Prior work has typically examined much smaller devices aimed at micro-electronics cooling applications whereas the present work aims to improve understanding of larger scale devices for incorporation in solar collectors and multi-function climate control building envelopes. Such applications can facilitate local renewable energy generation (solar and ambient heat collection) and improve cooling system energy efficiency (passive heat rejection) in order to address the climate crisis by decarbonising built environment energy use. Experimental work involved a horizontally oriented PLVTD formed of two parallel isothermal plates with integral serpentine heat exchangers and external insulation. Plate, fluid, and ambient temperatures were controlled and measured to determine heat transfer coefficients under various temperature difference and heat flux operating scenarios in order to validate a simple one-dimensional lumped parameter model.

Measured forward mode heat transfer $150<U_f<500$ $W \cdot m^{-2}K^{-1}$ combined with reverse mode insulation $U_r=10$ $W \cdot m^{-2}K^{-1}$ corresponds $\varsigma \approx 88\%$ diodicity at low condenser temperatures and fluxes ($T_2 \approx 15°C$ and $q/A \approx 120$ $W \cdot m^{-2}$) and $\varsigma \approx 96\%$ at high condenser temperatures and heat fluxes ($T_2 \approx 60°C$ and $q/A \approx 2800$ $W \cdot m^{-2}$). Forward mode performance increases with increasing heat flux and (to a lesser extent) with increasing operating temperature but is largely independent of PLVTD dimensions. Reverse mode performance is largely independent of heat flux and temperature but reduces (improves thermal insulation) with increasing cavity depth. The model has been used to show that a stainless steel PLVTD with x=70mm cavity can achieve $U_r=2$ $W \cdot m^{-2}K^{-1}$ with similar forward mode performance to the experimental prototype. Such a device would achieve diodicity of $\varsigma>97\%$ and be suitable for application in solar collectors and climate control building envelopes.

1 Introduction

A thermal diode is a unidirectional heat transfer device that operates in a manner analogous to an electrical semiconductor diode by offering low resistance (thermal conductance) in one direction and high resistance (thermal insulation) in the other. The broad concept of a "Thermal diode" and the ideas of "Thermic diodicity" and "Thermal Rectification" have been examined by a number of authors (Go & Sen, 2010; Roberts & Walker, 2011; Boreyko et al., 2011; Ben-Abdallah & Biehs, 2013; Dos Santos Bernardes, 2014; Bairi et al., 2014; Pei et al., 2017). Many of the aforementioned studies relate to thermal rectification using asymmetric solid material conduction, surface radiation, or natural convective thermosyphon arrangements rather than liquid-vapour phase change, but the definitions are equally applicable irrespective of the heat transfer mechanisms involved. A key parameter describing the effectiveness of a thermal diode is its diodicity (ς), for which several definitions are found in the literature. The definition preferred by the present authors is the "diodicity coefficient" which conveniently scales the degree of rectification between zero and unity. Diodicity coefficient (Equation 1) is defined in terms of the apparent thermal conductivity (k) of the diode in forward (f) and reverse (r) modes but can alternatively be written in terms of thermal power (q), heat flux (q/A), thermal conductance (U), or thermal resistance (R) where the dimensional quantities x and A relate to the depth and surface area of the diode with A=yz applying in the case of a rectangular flat plate diode of the form shown in Figure 1.

$$\boldsymbol{\varsigma} = \frac{\boldsymbol{k_f - k_r}}{\boldsymbol{k_f + k_r}} \qquad (0 \geq \varsigma \geq 1) \qquad \textbf{Equation 1}$$

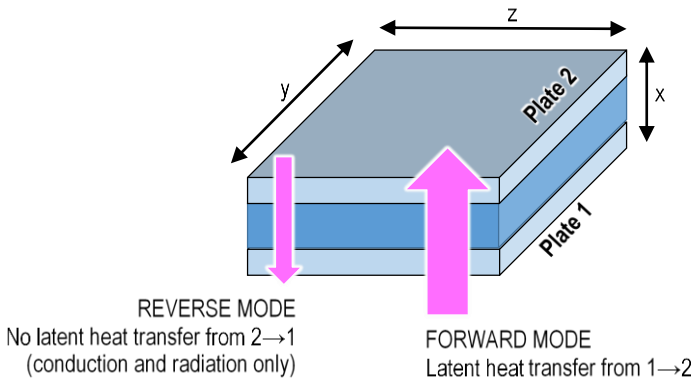

Figure 1 – Schematic diagram of a horizontal PLVTD

As indicated in Figure 1, a Planar Liquid-Vapour Thermal Diode (PLVTD) realises thermal diodicity by enabling latent transfer (evaporation, vapour mass flow, and condensation) in forward mode and by preventing latent heat transfer in reverse mode. The two operating modes are illustrated in Figure 2 and explained in more detail below. High rates of heat transfer occur during steady state forward mode operation when latent heat transfer processes are enabled because:

- Plate 1 is wetted by the liquid working fluid, and;
- Plate 1 is hotter than Plate 2 and hotter than the working fluid saturation temperature so that evaporation occurs, and;
- Plate 2 is cooler than Plate 1 and cooler than the working fluid saturation temperature so that condensation occurs.
- Working fluid vapour mass flows across the cavity from Plate 1 to Plate 2, primarily driven by the saturation pressure differential, but also in part by natural convection resulting from the density differential and gravity (buoyancy effects).
- Working fluid liquid returns from Plate 2 to Plate 1. In the simple horizontally oriented PLVTD featured in this study, condensate returns as drips driven by gravity. In PLVTD concepts which operate in vertical or tilted orientations, condensate flow returning to the evaporator must overcome gravity by utilising a capillary wick (Smyth, 2017), mechanical pump (Pugsley et al., 2016), or other driver such as surface wettability gradient (Boreyko and Chen, 2013) or applied electrostatic force (Traipattanakul et al., 2019).

Much lower rates of heat transfer occur during steady state reverse mode operation because Plate 2 is not wetted, meaning that no evaporation can occur, and thus no

latent heat flows between the plates. Residual sensible heat transfer between the plates occurs in reverse mode due to:

- Natural buoyant convection and gaseous conduction associated with working fluid vapour (and non-condensable gases, if present) in the cavity.
- Conductive heat transfer through the diode sidewalls and supporting structure.
- Radiative heat transfer between the two plate surfaces.

The PLVTD's diodicity relies upon ensuring that the working fluid circulation arrangement continually wets Plate 1 in forward mode and enables Plate 2 to remain dry in reverse mode. Inadvertent wetting of Plate 2 during reverse mode operation will facilitate latent heat transfer that will undermine the insulation performance and significantly diminish the diodicity.

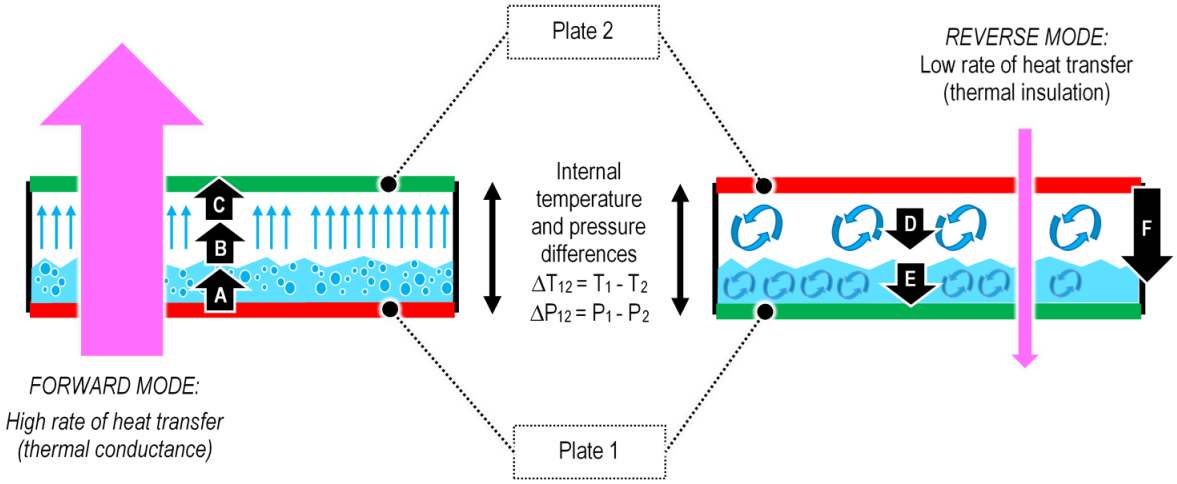

Key to annotations

A) Evaporation of the working fluid due to heat input at temperature T_1

B) Working fluid vapour mass transfer across cavity due to pressure difference $\Delta P_{12} = P_1 - P_2$. The working fluid exists in a condition close to the liquid-vapour saturation point. The average vapour pressure (P_{Lv}) corresponds to the saturation temperature (T_{Lv}) which is approximately equal to the average operating temperature $T_{12} = (T_1 + T_2) / 2$

C) Condensation of the working fluid produces heat output at temperature T_2

D) Buoyancy induced working fluid vapour convection due to temperature difference $\Delta T_{12} = T_1 - T_2$

E) Buoyancy induced working fluid liquid convection

F) Residual heat transfer via radiation between plates and conduction through sidewalls and structural elements

Figure 2 – Heat transfer mechanisms in a Planar Liquid-Vapour Thermal Diode

Thermal diodes are well suited to electronics cooling applications (Boreyko and Chen, 2011 & 2013; Chen et al., 2012; Blet et al., 2017; Avanessian and Hwang, 2018; Traipattanakul et al., 2019; Wong et al., 2019), solar collector applications (De Beijer, 1998; Quinlan, 2010; Souliotis et al., 2011&2017; Smyth et al., 2015a&b, 2017, 2018, 2019; Pugsley et al., 2016; Pugsley, 2017; Muhumuza et al., 2019a & b), climate control building envelopes (Chen et al., 1998; Varga, 2002; Reay et al., 2014; Villeneuve et al., 2017), and permafrost stabilisation applications (Pan and Wu, 2002; Pei et al., 2017). Applications in spacecraft (Gaddam and Huxtable, 2017) and caloric refrigeration systems (Hess et al., 2019), and thermal computing (Tso and Chao, 2016; Shen et al., 2018) have also been proposed. The majority of extant published work on liquid-vapour phase change thermal diodes relates to either axial devices (eg heat pipes), annular devices (eg cylindrical or elliptical tanks), or small planar devices (eg jumping drop diodes).

Wong et al. (2019) examined an axial liquid-vapour thermal diode with small circular heat transfer plates (equal evaporator and condenser areas $A_e=A_c=0.01m^2$) oriented horizontally and separated by a relatively large cavity (x=76mm). The device is superficially similar to a wickless heat pipe, and essentially similar to the PLVTD described in Figures 1 and 2, relying upon gravity to induce the return flow of condensate from the condenser to the evaporator pool. Tests demonstrated that the device achieved forward and reverse mode thermal conductances of $U_f\approx40\ W\cdot m^{-2}K^{-1}$ and $U_r\approx16\ W\cdot m^{-2}K^{-1}$ corresponding to diodicity of $\varsigma\approx43\%$. Reverse mode heat transfer appears to be mainly governed by conduction whereas forward mode heat transfer is governed by buoyant natural convection (thermosyphonic action of air and water) and boosted by liquid-vapour-liquid phase change (latent heat transfer).

Smyth et al. (2017 & 2018) and Muhumuza et al. (2019a & b) examined various cylindrical solar water heaters featuring annular liquid-vapour thermal diodes. Early prototypes were oriented vertically whilst more recent evolutions have been horizontal such that the thermal diode operates broadly similarly to Figure 3a with condensate return via gravity. According to Quinlan (2010), Smyth et al. (2017) and Pugsley (2017), the "Mark IV" was formed of a 300mm diameter, 1000mm long, cylindrical outer vessel and a 200mm diameter, 900mm long, inner vessel arranged concentrically to form an annulus cavity of x=50mm. During heat collection (forward mode) wetted pockets on the inner surface of the outer vessel act as evaporators ($A_e\approx0.5m^2$) transferring latent heat in the form of vapour which condenses on the outer surface of the inner vessel ($A_c\approx0.6m^2$). During heat retention (reverse mode) the annulus acts as an insulator because the outer surface of the inner vessel is kept dry. Test results showed that the annular thermal diode achieved forward and reverse mode heat transfer $U_fA\approx13\ W\cdot K^{-1}$ and $U_rA\approx1.3\ W\cdot K^{-1}$ corresponding to diodicity of $\varsigma\approx82\%$.

Comprehensive work on planar liquid-vapour thermal diodes was undertaken by Boreyko and Chen (2011 & 2013) who developed, tested and modelled a PLVTD of similar form to that illustrated in Figures 1 and 2. A key innovation in their device was the use of a superhydrophobic condenser and a superhydrophilic wicked evaporator to enable the working fluid to return from the condenser to the evaporator via the "jumping drop" phenomenon. This feature gave the device gravity-independent operation enabling it to function in any orientation (horizontal, vertical or tilted) which is important for its primary application in mobile electronic devices, but also relevant to solar collectors and building envelopes. Experimental work utilised a small prototype consisting of two square copper plates (A_e=A_c=0.006m^2) separated by an EPDM gasket (various thicknesses up to x=4mm) and achieved forward and reverse mode thermal conductances of U_f=40500 W·m^{-2}K^{-1} and U_r=165 W·m^{-2}K^{-1} corresponding to diodicity of ς=99%. Using a similar but smaller device (A_e=A_c=0.0012m^2), Traipattanakul et al. (2019) explored the possibility of using an electric field to enable jumping drop action across a wider separation of the diode plates (x=7mm) to enable lower reverse mode performances. The work successfully proved the concept, but the relatively small plate-to-plate cavity width (x) limited the overall thermal insulation values to only ~10 W·m^{-2}K^{-1} which is an order of magnitude greater than typically required for solar collector and building envelope applications.

All of the abovementioned experimental studies used water as the working fluid to facilitate the latent heat transfer, and with the exception of the work by Wong et al. (2019), all utilised cavity evacuation to remove non-condensable gases and facilitate low temperature evaporation of water at sub-atmospheric pressures. Boreyko and Chen (2013) demonstrated clearly that forward mode heat transfer is maximized when non-condensable gases are removed such that the cavity pressure approaches the saturation pressure of the working fluid.

The most basic realization of a PLVTD is the horizontally oriented form shown in Figure 2 whereby Plate 1 is permanently wetted by a pool of liquid working fluid which covers the evaporator surface. Condensate forms on Plate 2 when forward mode heat transfer occurs and this liquid flows back to Plate 1 due to gravity so that operation can continue indefinitely. This form of PLVTD could feasibly be used as a heat transfer element in a concentrating solar water heater (see Figure 3a) or as a flat roofing panel for buildings in hot climates where daytime solar gain control and night-time free-cooling are required (see Figure 3b).

The study presented in this paper aims to build upon the aforementioned studies by improving understanding of large scale PLVTDs. Prior work on PLVTDs has generally been focussed on small devices with evaporator and condenser plate areas of $A \leq 0.01m^2$ and cavity depths of $x \leq 7mm$ which, whilst relevant to micro-electronics cooling applications, are of limited direct relevance to solar collector and multi-function climate control building envelope applications. Prior work on larger scale thermal diodes has generally focussed on devices with inherently axial or annual forms which differ significantly from the flat plate form of a true PLVTD. This study describes pioneering work to experimentally measure the heat transfer characteristics of a $0.15m^2$ PLVTD under various realistic operating conditions and presents a corresponding validated one-dimensional lumped parameter heat transfer model.

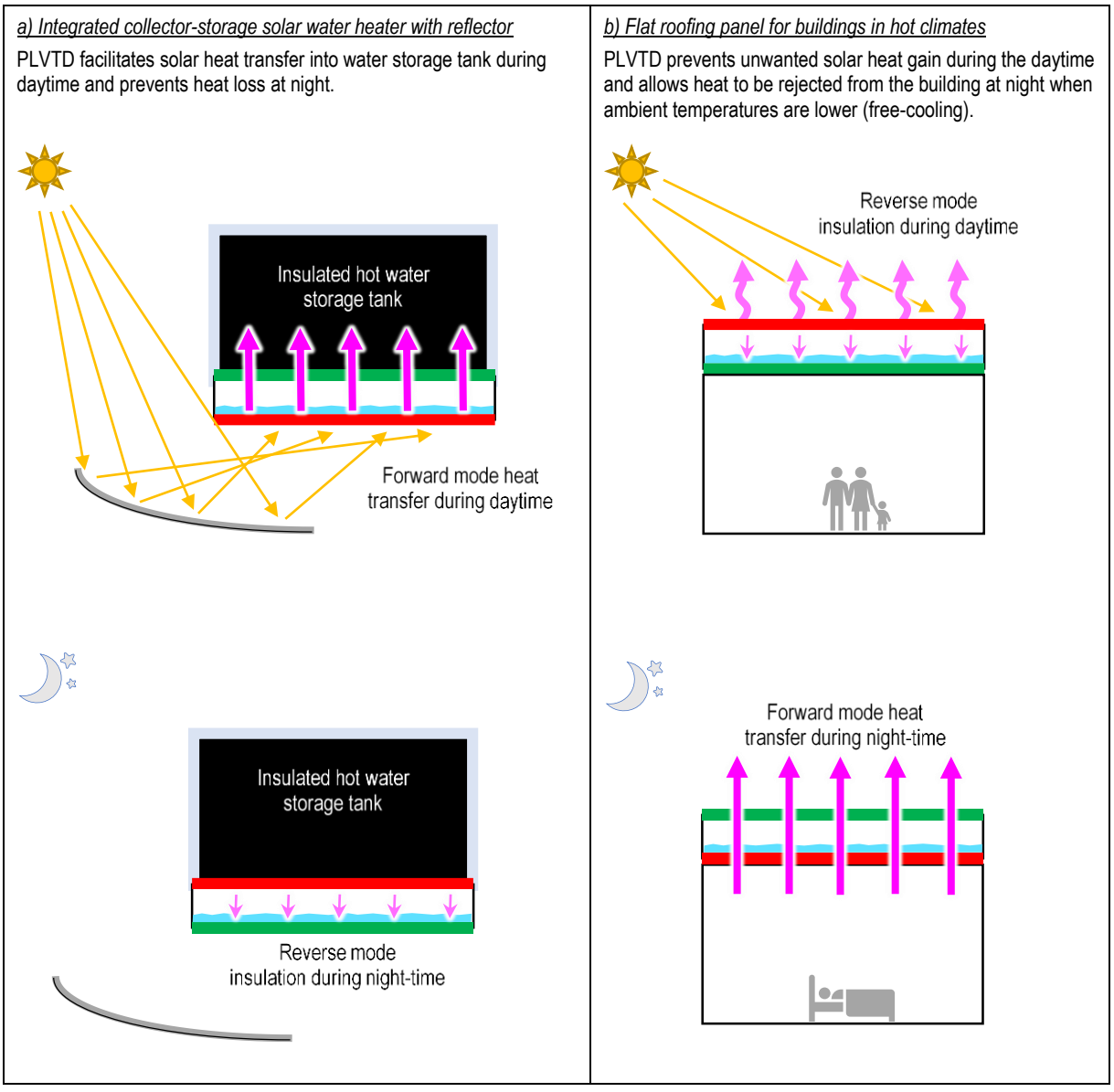

Figure 3 – Practical applications for a horizontal PLVTD

2 Theoretical model

2.1 Heat flux, temperature and pressure

Heat transfer is driven by the difference in temperature between the two plates (ΔT_{12}). The transferred thermal power (q_{12}), transferred heat flux (q_{12}/A_p), overall thermal resistance (R_{fr}), and overall thermal conductance (U_{fr}) through the PLVTD are related according to Equation 2. Figure 4 shows the main heat transfer paths and corresponding thermal resistances through a PLVTD in both forward and reverse mode.

$$U_{fr} = \frac{q_{12}}{yz(T_1 - T_2)} = \frac{q_{12}}{A_p \Delta T_{12}} = \frac{1}{A_p R_{fr}} \quad \text{Equation 2}$$

In forward mode, the dominant thermal transmission mechanism is latent heat transfer associated with working fluid liquid-vapour-liquid phase changes and the net transfer of working fluid vapour mass across the cavity between the two plates. In reverse mode, thermal transmission occurs via several different mechanisms including working fluid natural convection (vapour and liquid without phase change), radiation across the cavity, and conduction through the envelope and supporting structural elements, but no latent heat transfer occurs. In order to transfer heat in forward mode the working fluid must exist in vapour phase at the evaporator temperature (T_1) and in liquid phase at the condenser temperature (T_2). If all non-condensable gases are removed, then the resulting pressure inside the PLVTD will be approximately equal to the saturation pressure (P_{Lv}) of the working fluid at the average operating temperature $T_{12}=(T_1+T_2)/2$. This internal pressure will usually be different from the atmospheric pressure outside necessitating internal structures to ensure that the PLVTD envelope can withstand the pressure differential (hence need for supporting structure).

2.2 Thermal resistance lumped parameter model

The total thermal resistance associated with latent heat transport (R_{LvL}) through the working fluid can be defined as the sum of individual evaporation (R_e), vapour mass flow (R_{ec}), and condensation (R_c) components acting in series. Thermal resistance R_{LvL} is inherently much lower than the sum of the series thermal resistances associated with sensible heat transport through the working fluid in its liquid (R_L) and vapour (R_v) forms (ie natural convection without phase change). Thermal resistances associated with conduction through the two plates ($2R_p$) act in series with the aforementioned components, whereas thermal resistances associated with radiation between the plates (R_R), conduction through the sidewalls (R_w), and conduction through structural support elements (R_S) act in parallel. Inspection of the resulting thermal resistance network in Figure 4c suggests that the overall thermal resistance through the PLVTD during forward mode operation (R_f) can be approximated by Equation 3.

a) Forward mode thermal resistance

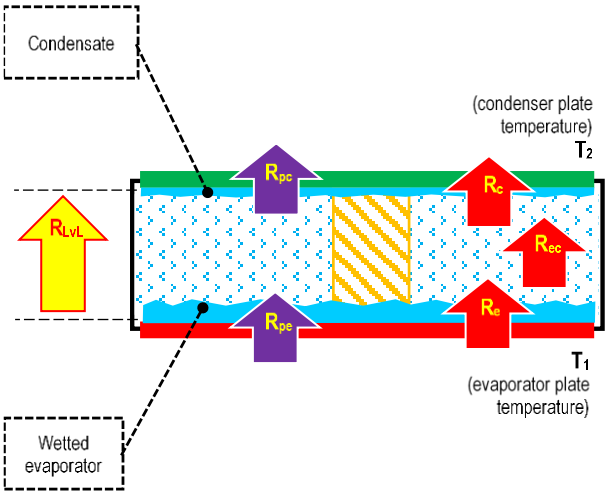

b) Reverse mode thermal resistances

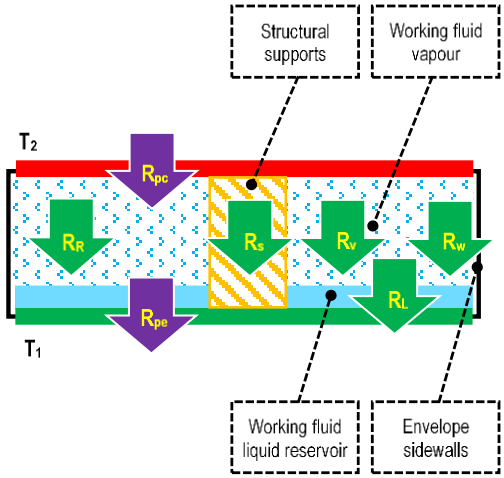

c) Thermal resistance network describing heat transfer behaviour

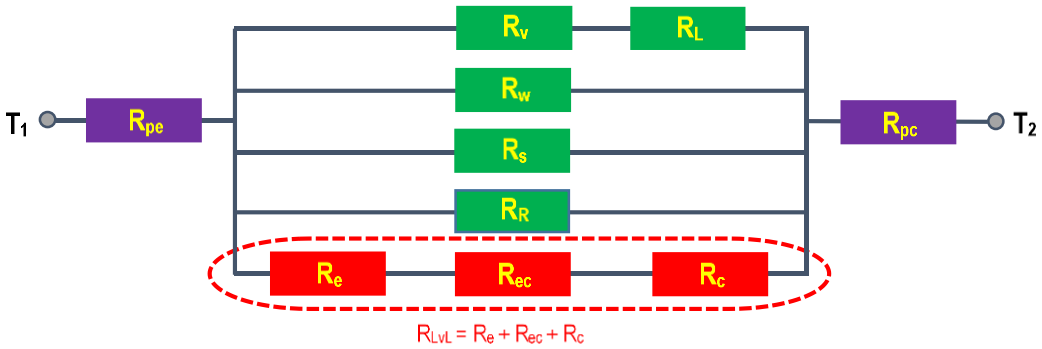

d) Descriptions of thermal resistances used in the model

R_{pe}	Conductive thermal resistance through the plate which acts as the evaporator in forward mode	R_w	Conductive thermal resistance through four sidewalls forming the PLVTD envelope
R_{pc}	Conductive thermal resistance through the plate which acts as the condenser in forward mode	R_s	Conductive thermal resistance through the structural members which support the PLVTD envelope
R_e	Resistance associated with working fluid evaporation occurring at the evaporator surface	R_v	Resistance associated with vapour phase natural convection of the working fluid
R_c	Resistance associated with working fluid condensation occurring at the condenser surface	R_L	Resistance associated with Liquid phase natural convection of the working fluid
R_{ec}	Mass transfer resistance associated with the flow of vapour from the evaporator to the condenser	R_R	Resistance associated with heat transfer via long wave electromagnetic radiation between the two plates
R_{LvL}	Overall Liquid-vapour-Liquid phase change heat transfer resistance		

Figure 4 – Forward and reverse mode heat transfer paths with corresponding thermal resistance network

The evaporator plate is dry in reverse mode so that the latent heat transport thermal resistances tend towards infinity and $1/(R_e+R_{ec}+R_c)\rightarrow 0$. Inspection of the thermal resistance network then yields Equation 4 to describe the overall thermal resistance through the PLVTD during reverse mode operation (R_r).

$$R_f = 1/\left(\frac{1}{R_e+R_{ec}+R_c}+\frac{1}{R_w}+\frac{1}{R_s}+\frac{1}{R_R}\right)+2R_p \quad \text{Equation 3}$$

$$R_r = 1/\left(\frac{1}{R_L+R_v}+\frac{1}{R_w}+\frac{1}{R_s}+\frac{1}{R_R}\right)+2R_p \quad \text{Equation 4}$$

2.3 Envelope, structure, and radiation thermal resistances

The envelope and structure thermal resistances can be evaluated using conventional Fourier methods. Assuming that the PLVTD envelope is of a basic rectangular box form (as per Figure 1) and the internal supporting structure is an array of cylindrical struts similar to that used in vacuum glazing panels (Collins and Fischer-Cripps, 1991; Fang et al., 2014) the thermal conductances and corresponding resistances of the evaporator and condenser plates ($U_{pe} \approx U_{pc}$), the envelope sidewalls (U_w), and the supporting structure (U_S), can be evaluated according to Equations 5 to 9. The nomenclature used for the various dimensional terms are defined in full in Section 9. The symbols U, R, k, A and d refer to thermal conductance, thermal resistance, thermal conductivity, area and distance respectively. The symbols and subscripts x, y, z refer to dimensions in the respective axes defined on Figure 1. The subscripts p, w, and s relate to the plate, wall and struts respectively. The term N_s refers to the number of struts in the internal supporting structural array where each strut is assumed to be a cylindrical tube with diameter d_s, wall thickness d_{sw}, and approximate length x. The term d_{ss} refers to the centre-to-centre spacing between adjacent struts and the terms d_{sxy} and d_{sxz} refer to spacings between struts and adjacent sidewalls.

$$U_p = \frac{1}{A_p R_p} = \frac{k_p}{x_p} \quad \text{Equation 5}$$

$$U_w = \frac{1}{A_p R_w} = \frac{2z_w(y+z-2z_w)k_w}{xyz} \quad \text{Equation 6}$$

$$U_s = \frac{1}{A_p R_s} = \frac{N_s A_s k_s}{xyz} \quad \text{Equation 7}$$

$$A_s = \pi\left(\frac{d_s}{2}\right)^2 - \pi\left(\frac{d_s-2d_{sw}}{2}\right)^2 \quad \text{Equation 8}$$

$$N_s = \left(\frac{y-2d_{sxy}}{d_{ss}}+1\right)\left(\frac{z-2d_{sxz}}{d_{ss}}+1\right) = \left(\frac{y-x}{d_{ss}}+1\right)\left(\frac{z-x}{d_{ss}}+1\right) \quad \text{Equation 9}$$

Radiative heat transfer resistance between the two parallel plates can be determined using Equation 10 (Twidell & Weir, 2006) based on the PLVTD absolute operating temperatures in Kelvin degrees (T_{12}), emissivities of the wet or dry plates (ε_1 and ε_2), the Stefan-Boltzmann constant (χ = 5.67 x 10^{-8} $W \cdot m^{-2}K^{-4}$) and the area over which radiative heat exchange occurs ($A \approx A_p$, assuming negligible wall thicknesses).

$$R_R = \frac{{}^1/_{\varepsilon_1} + {}^1/_{\varepsilon_2} - 1}{4\,\chi\,A\,(T_{12})^3} \qquad \textbf{Equation 10}$$

2.4 Evaporation, condensation and working fluid mass flow

Heat transfer through the PLVTD via the working fluid is dependent upon a number of different mechanisms:

- Sensible heat transfer via buoyancy driven natural convection of the working fluid, in both vapour (R_v) and liquid (R_L) states, in reverse mode, due to plate-to-plate temperature differential ΔT_{12}.
- Working fluid evaporation (R_e) in forward mode.
- Latent heat transfer due to net vapour mass flow between the plates in forward mode (R_{ec}). Fluid motion is primarily driven by the vapour pressure differential (ΔP_{12} arising from ΔT_{12}) and to a lesser extent by corresponding buoyancy forces.
- Working fluid condensation (R_c) in forward mode.

Working fluid thermal resistances and corresponding conductances can be evaluated using Equation 11 from appropriate Nusselt number correlations (Nu), characteristic dimensions (L) and working fluid thermal conductivities (k).

$$R = \frac{1}{A_p U} = \frac{L}{A_p\, k\, Nu} \qquad \textbf{Equation 11}$$

For sensible convective heat transfer through vapour within a horizontal PLVTD of the form shown in Figure 2 (relevant to evaluation of R_v) the Nusselt number is approximately Nu ≈ 1 during reverse mode operation because the hot surface is at the top of the cavity. The characteristic dimension is approximately equal to the cavity depth ($L \approx x$).

For sensible convective heat transfer through liquid within a horizontal PLVTD (relevant to evaluation of R_e and R_L) the Nusselt number can be evaluated using Equations 12 to 14 depending upon Rayleigh number and operating mode. Rayleigh numbers are typically evaluated using Equation 15 which accounts for buoyancy and frictional

effects based upon gravitational acceleration ($g=9.81$ m/s^2 at sea level), plate-to-liquid temperature difference ($\Delta T_{L1}=T_1-T_{12}$) and temperature dependent working fluid thermodynamic properties including kinematic viscosity (v), Prandtl number (Pr) and volumetric expansion coefficient (β) which should be evaluated at the liquid temperature $T_{L1}=(T_1+T_{12})/2$. The characteristic dimension is defined as the ratio of the plate area divided by the plate perimeter length according to Equation 16. In solar collector and climate control building envelope applications, the vaporisation process during forward mode occurs primarily as a result of free-surface evaporation because heat fluxes are low and resulting plate-to-liquid temperature differences are not large enough to facilitate nucleate boiling. Equations suited to modelling high heat flux operating scenarios and alternative PLVTD orientations (vertical, tilted, and inverted) are given by Pugsley (2017) but have been omitted here for brevity.

$$Nu = 0.54Ra^{0.25} \quad (\text{Forward mode for } 10^4 \leq Ra < 10^7) \qquad \textbf{Equation 12}$$

$$Nu = 0.15Ra^{1/3} \quad (\text{Forward mode for } 10^7 \leq Ra < 10^{11}) \qquad \textbf{Equation 13}$$

$$Nu = 0.27Ra^{0.25} \quad (\text{Reverse mode for } 10^5 \leq Ra < 10^{11}) \qquad \textbf{Equation 14}$$

$$Ra = \frac{g\,\beta\,\Delta T\,L^3}{v^2}Pr \qquad \textbf{Equation 15}$$

$$L = \frac{yz}{2(y+z)} \qquad \textbf{Equation 16}$$

For latent heat transfer caused by vapour mass flow and vapour convection during forward mode operation (relevant to evaluation of R_{ec}) the Nusselt number can be evaluated using Equation 17 (Cengel, 2006) which is appropriate to rectangular enclosures where the hot surface is at the bottom of the cavity and is valid for Prandtl numbers $0.1<Pr<10$ and Rayleigh numbers $Ra<10^8$. Whilst the Rayleigh number for sensible heat transfer is determined by considering buoyancy as the driving force (Equation 17), for latent heat transfer in forward mode, the Rayleigh number is additionally dependent upon the vapour pressure differential $\Delta P_{12}=|P_1-P_2|$ associated with the plate-to-plate temperature difference $\Delta T_{12}=|T_1-T_2|$. This phase change pressure differential provides the dominant driving force which, in addition to buoyancy force, overcomes the viscous and frictional forces associated with vapour convection. Methods for determining modified Rayleigh (Ra^*) numbers appropriate for evaluating vapour mass transfer thermal resistance in phase change scenarios (both with and without non-condensable gases present) were proposed by Pugsley (2017) drawing on the work of Stein et al. (1985) and Peterson (1996). Equations 18 to 20 can be used

in cases where all non-condensable gases have been removed such that the PLVTD cavity exists at the working fluid saturation pressure (P_{LV}) corresponding to the average temperature $T_{12} = (T_1+T_2)/2$. The terms h_{Lv}, ϑ, $\mathcal{M}$, and $\mathcal{R}$ are the latent heat of phase change, thermal diffusivity, working fluid molar mass, and universal gas constant respectively. All thermodynamic properties in Equations 18 to 20 (k, v, ϑ, β, ρ) relate to the vapour state which exists at a temperature close to that of the average of the two plates ($T_v \approx T_{12}$). In the case of vapour flowing due to phase changes, the effective thermal conductivity (k of Equation 11) has both sensible vapour (k_v) and latent (k_{Lv}) components which can be quantified using Equation 19 and 20.

$$Nu = 1 + 1.44\left[1 - \frac{1708}{Ra}\right]^{+} + \left[\frac{Ra^{1/3}}{18} - 1\right]^{+} \quad \textbf{Equation 17}$$

$$Ra^{*} = \frac{\left[\frac{P_{Lv}}{\rho_L} + g\right]\beta\, \Delta T_{12}\, L^3}{v^2} Pr \quad \textbf{Equation 18}$$

$$k = k_v + k_{Lv} \quad \textbf{Equation 19}$$

$$k_{Lv} = \frac{{h_{Lv}}^2\, P_{Lv}\, \mathcal{M}^2\, \vartheta}{\mathcal{R}^2\, {T_{12}}^3} \quad \textbf{Equation 20}$$

Heat transfer due to condensation on the underside of the top plate during forward mode operation (relevant to evaluation of R_c) can be evaluated using Equations 21 and 22 which are based on expressions given by Gerstmann & Griffith (1967) and by Stein et al. (1985). The difference in the liquid and vapour densities (ρ_L and ρ_v) plays an important role in both expressions alongside the liquid kinematic viscosity (v_L), surface tension (σ_L), and thermal conductivity (k_L). Vapour thermodynamic properties and saturation condition thermodynamic properties can be evaluated at the estimated saturation temperature ($T_{Lv} \approx T_{12}$). Liquid condensate thermodynamic properties can be evaluated at the estimated condensate film temperature $T_{L2}=(T_{12}+T_2)/2$.

$$Ra = \frac{g\,(\rho_L - \rho_v)\, h_{Lv}\left(\frac{\sigma_L}{g\,(\rho_L - \rho_v)}\right)^{1.5}}{k_L v_L (T_{Lv} - T_2)} \quad \textbf{Equation 21}$$

$$R_c = \frac{\left(\frac{\sigma_L}{g\,(\rho_L - \rho_v)}\right)^{0.5}}{A_p\, k_L\, 0.69\, Ra^{0.2}} \quad \textbf{Equation 22}$$

3 Experimental apparatus and methodology

The experimental methodology largely followed the precedent set by the work of Boreyko & Chen (2013) but using apparatus with larger plate area dimensions (to better reflect the sizes of relevance to solar collector and climate control building envelope applications) and without special treatments to the evaporator or condenser surfaces (aluminium plates with standard mill finish). Steady state temperatures and heat fluxes were achieved by circulating heated and chilled water through channels located within the body of the evaporator and condenser plates. The specific objectives of the experimental investigation were to quantify the effects of varying the:

- Reverse mode plate-to-plate temperature differential in the range $5<\Delta T_{12}<70$°C corresponding to nominal plate temperatures of $20<T_2<75$°C and $5<T_1<15$°C.
- Forward mode heat fluxes in the range $100<q/A<6000$ W·m^{-2} corresponding approximately to plate-to-plate temperature differences of $1<\Delta T_{12}<10$°C.

Photographs of the PLVTD used for the experimental investigation are shown on Figures 5 and 6. The key components included:

- Spacer frame (A) acted as the sidewalls forming the PLVTD cavity. Several different spacer frames were fabricated using a CNC controlled water-jet cutting machine. Test results presented in this paper were undertaken using an 11mm thick nylon spacer which was found to provide superior reverse mode (insulation) performance owing to its low thermal conductivity.
- Two heat transfer plates (B1 & B2) which acted as the evaporator and condenser, each consisting of a 300x500 mm piece of 12 mm thick aluminium plate which was chosen for its relatively high thermal conductivity at relatively low cost. Each plate was CNC machined to have a parallel flow serpentine water flow channel (4 x 4 mm x 7m long) on one side and a perimeter groove on the other side to accommodate an O-ring vacuum seal. The chosen plate size was primarily determined by the constraints of the CNC machine. The plate surfaces forming the evaporator and condenser were not machined (standard smooth, dull, mill finish) but were cleaned using isopropyl alcohol to remove any grease.
- Two water-side cover plates (B3 & B4) each consisting of a 300x500 mm piece of 6mm thick aluminium plate. Holes were drilled to accommodate vacuum fittings, water supply connections, and clamping bolts.

Figure 7 shows a schematic of the PLVTD test apparatus, consisting of the insulated PLVTD (components A, B & C), the measurement datalogger (D), the hot and cold water supply system (E & F) and the vacuum pump system (G). The datalogger monitored flow rates (M), temperatures (T) and cavity pressure (P). The horizontal orientation of the PLVTD assembly (A, B, C) was verified using a digital inclinometer prior to tests.

Non-condensable gases were removed from the PLVTD cavity using the vacuum pump before and after injection of the working fluid through the fill point. The working fluid consisted of 0.28L de-ionised water corresponding to approximately 2.5kg/m^2 of evaporator surface area. Cavity pressures were monitored throughout the tests and maintained at <25% above the expected saturation pressure by repeating evacuation (prior to, but not during, each measurement) to remove the small amounts of non-condensable gas which arose from air infiltration and outgassing. Slight loss of working fluid due to repeated evacuations was observed (0.26L remaining after several days of testing) but is not considered significant.

During each test, heat was supplied to one of the PLVTD plates from the water heating circuit and removed from the other plate by the chilled water circuit. The two circuits each featured insulated flexible pipework, one oval gear flow meter (M) and two variable speed pumps which were arranged in series in order to overcome the high pressure drop imposed by the water flow channels within each plate. An arrangement of gate valves was used to regulate flow rates and to determine operating mode such that, in forward mode, the evaporator was connected to the heating circuit and the condenser was connected to the chilling circuit. Valve settings were inverted during reverse mode operation to enable the plates to be connected the opposite way around. Additional valves allowed the system to be filled or flushed with water from the mains supply or drained down. Temperatures, flow rates and pressures were continuously recorded throughout the experiments using the datalogger set to have a 1 minute sampling time. Calibration checks indicated that the accuracy of temperature readings provided by the thermocouples was ±1.0°C for temperature readings indicated by any one thermocouple and ±0.3°C for temperature differences derived from readings indicated by a pair of thermocouples. The uncertainty associated with the flow rate readings was found to be ±9% for volume flow rates of water in the range 100 to 1000 mL/min at temperatures in the range 5 to 75°C.

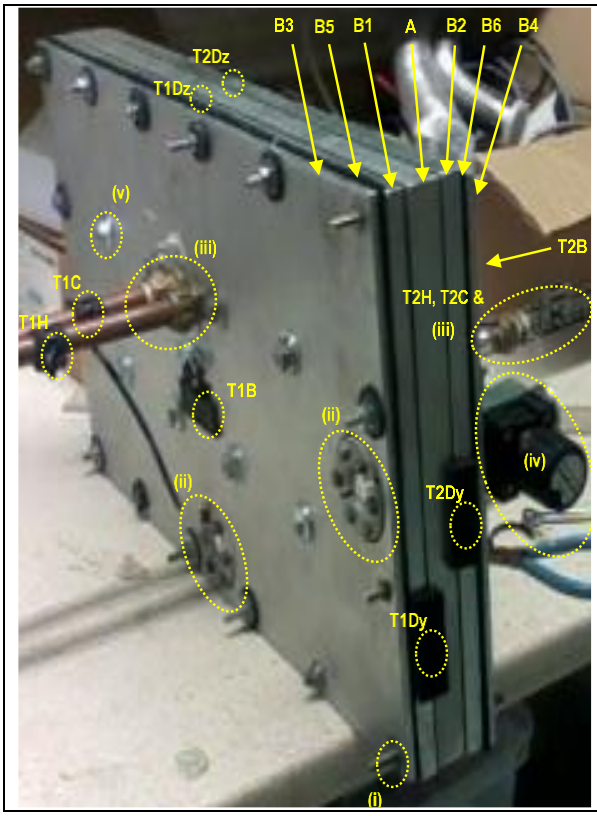

Key to annotations

A	Spacer frame
B1&2	Heat transfer plates
B3&4	Water-side cover plate
B5&6	Gasket sheet to seal water channels
i	Perimeter clamping bolts & insulating washers
ii	Vacuum port with blank flange
iii	Water inlet and outlet ½" BSP
iv	Vacuum port with KF16 Speedivalve
v	Cover plate bolts, nuts and washers
T_{1H}& T_{1C}	Thermocouples to monitor inlet and outlet water temperatures of heat transfer plate 1
T_{2H}& T_{2C}	Thermocouples to monitor inlet and outlet water temperatures of heat transfer plate 2
T_{1B}& T_{2B}	Thermocouples monitoring temperatures at centre back cover of each heat transfer plate
T_{1Dz}& T_{2Dz}	Thermocouples monitoring temperatures along long edge of each heat transfer plate
T_{1Dy}& T_{2Dy}	Thermocouples monitoring temperatures along short edge of each heat transfer plate

Figure 5 – Annotated photograph of the assembled prototype PLVTD

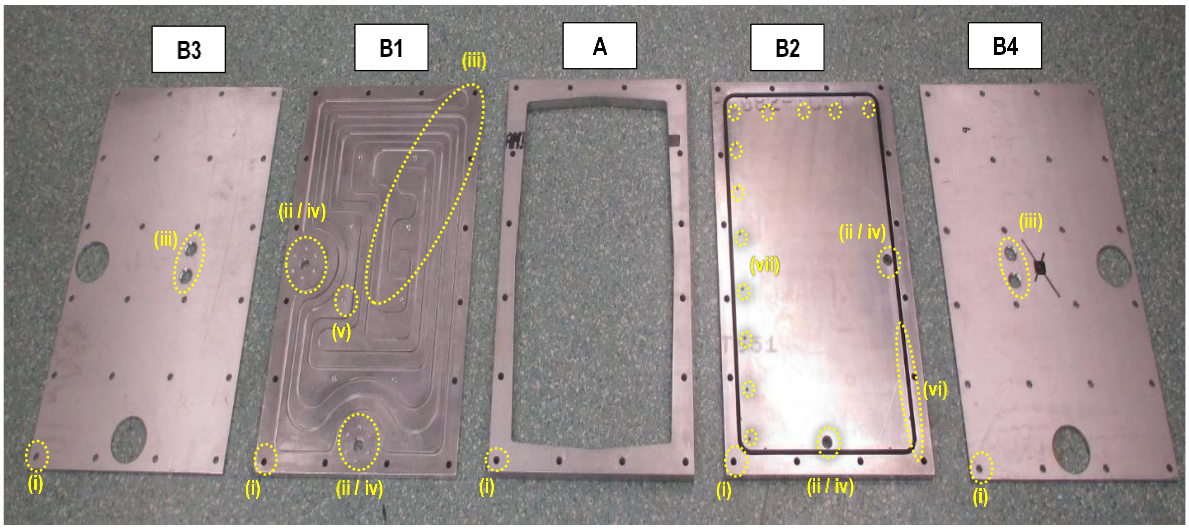

Key to annotations

A	Spacer frame
B1 & B2	Heat transfer plate (12 mm aluminium). Both plates are identical but opposite sides are shown in the photograph.
B3 & B4	Cover plate (6 mm aluminium).
i to v	Holes for fixtures and fittings. Refer to Figure 5 for details.
vi	Viton cylindrical section O-ring seal 5.3mm x 430mm.
vii	Fixing holes for internal ancillary components (not used).

Figure 6 – Annotated photographs showing main component parts of the prototype PLVTD before assembly

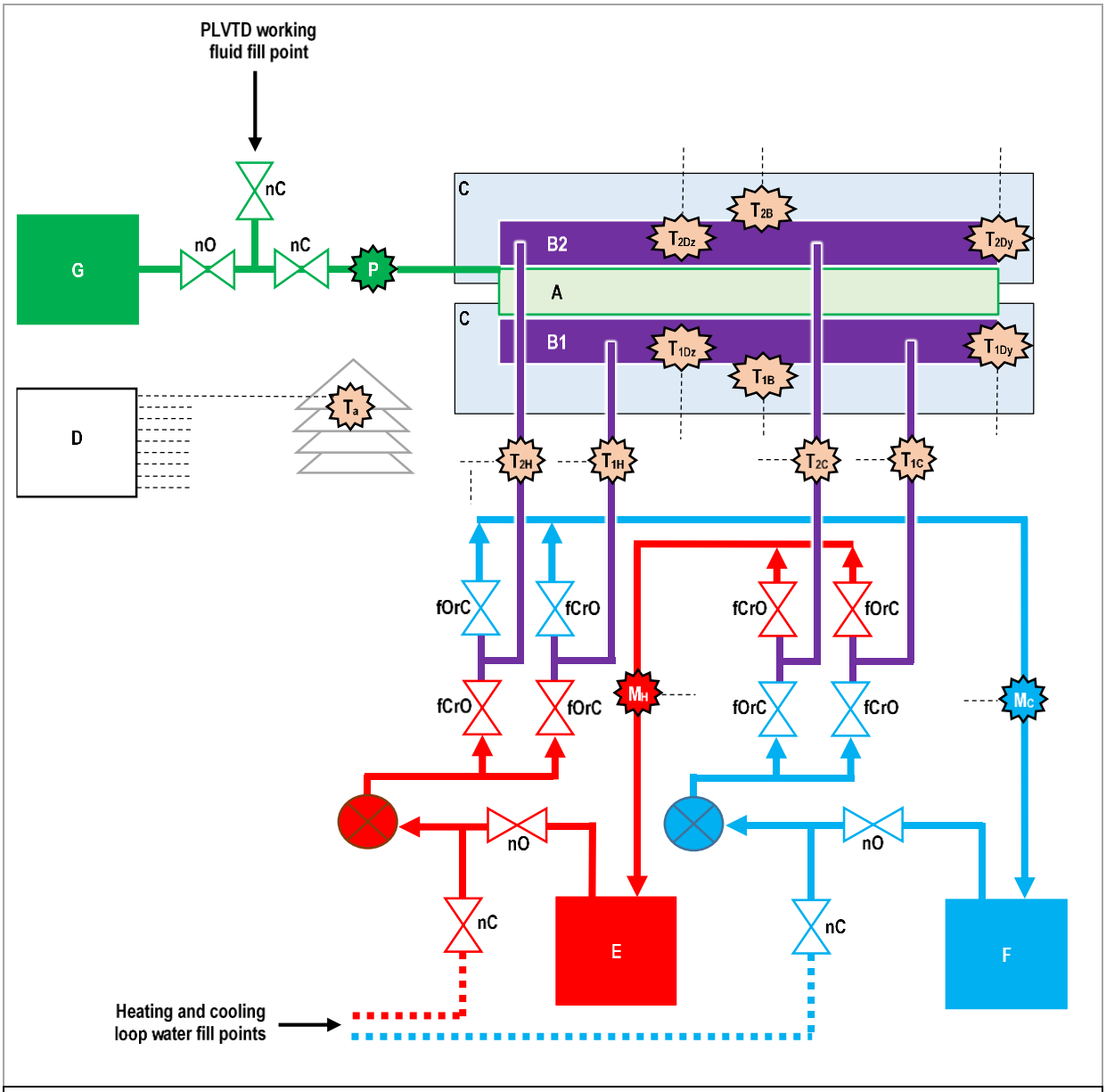

Key to annotations:

A	Spacer frame
B	Heat transfer plates and covers
C	50 mm polystyrene foam insulation
D	DeltaT DL2e datalogger connected to computer
E	Julabo ED19A heating circulator
F	Julabo F33MA refrigerated-heating circulator
G	Edwards XDS5 scroll vacuum pump

Wilo 4035479 SB30 water circulating pumps in series

Gate valves, operation denoted by codes:

fOrC	Open in forward mode, Closed in reverse mode
fCrO	Closed in forward mode, Open in reverse mode
nO	Normally Open, except during filling
nC	Normally Closed, except during filling

Measurement point, denoted by one of the following letters:

M	Mass flow rate measurement using Nixon OG1 oval gear flow meter
P	Vacuum pressure measurement using Edwards CG16K, Digitron 2025P & Druck DPI-104 gauges
T	Temperature measurement using T-type thermocouples on the hot (T_H) and cold (T_C) pipe connections, at the back (T_B) and edges (T_{Dy} & T_{Dz}) of the plates, and local ambient (T_a)

Figure 7 – Test apparatus used for the PLVTD experimental investigation

The heating and chilling circuit supply temperatures and flow rates determined the amount of thermal power available for transfer through the PLVTD prototype and hence also controlled the evaporator and condenser plate temperatures. The amount of heat supplied (q_{HC}) or removed (q_{CH}) by each plate was determined from Equations 23 and 24 respectively accounting for the inlet-to-outlet temperature differences ($\Delta T_{HC}=T_H-T_C$ when supplying heat or $\Delta T_{CH}=T_C-T_H$ when removing it), the fluid mass flow rates fed through the plates (M_{HC} and M_{CH} respectively) and the specific heat capacity of that fluid (c_p) at its average temperature $T_{HC}=(T_H+T_C)/2$. Heat supplied by one plate (q_{HC}) should always be equal to the amount of heat removed by the other plate ($-q_{CH}$) if ambient losses are properly accounted for. The amount of heat lost (q_l) from a hot plate to the ambient environment (or gained from ambient by a cold plate) can be determined according to Equation 25 based on the back-of-plate temperature (T_B), the edge-of-plate average temperature ($T_D=0.5T_{Dy}+0.5T_{Dz}$) the ambient temperature (T_a) and the heat loss thermal resistance (R_l). In order to obtain reliable measurement data, the inlet-to-outlet temperature differences (ΔT_{HC} and ΔT_{CH}) and plate-to-plate temperature difference (ΔT_{12}) need to be higher than the ±0.3°C uncertainty associated with such measurements. Temperature differences of 1.2°C would theoretically have an uncertainty of ±25%. The magnitude of the plate-to-plate temperature difference is dependent upon the heat flux flowing through the PLVTD ($q_{HC}/A_p \approx -q_{CH}/A_p$) and the overall thermal conductance (U_{fr}) of the PLVTD as described by Equation 26.

$$q_{HC} = M_{HC}\, c_{p,HC}\, \Delta T_{HC} - q_{lHC} \qquad \textbf{Equation 23}$$

$$q_{CH} = M_{CH}\, c_{p,CH}\, \Delta T_{CH} - q_{lCH} \qquad \textbf{Equation 24}$$

$$q_l = \frac{0.5\,(T_B + T_D) - T_a}{R_l} \qquad \textbf{Equation 25}$$

$$\Delta T_{12} = \frac{0.5\,(q_{HC} - q_{CH})}{U_{fr}\, A_p} \qquad \textbf{Equation 26}$$

4 Measurement results and model validation

Figure 8 shows an example temperature, pressure and flow rate time history measured during one set of forward mode tests. Numbered labels show five condenser plate temperature setpoints corresponding to approximately T_2=15, 25, 35, 45 and 50°C.

Steady state temperatures were typically achieved about half an hour after each setpoint change. Flow rates were maintained broadly constant at $M_{HC}=M_{CH}=0.65\pm0.1$ L/min throughout the tests. Measured pressures (P_{meas}) increased with increasing temperature and corresponded broadly to saturation pressure estimates ($P_{Lv(HCCH)}$) which were evaluated from the average flow and return temperatures using REFPROP software (NIST, 2013). Figure 9 shows the corresponding derived thermal powers ($q_{HC} = -q_{CH} = 400\pm30$ W throughout the featured tests) and thermal conductances which rose from $U_f = 300$ W·m^{-2}K^{-1} at the lowest operating temperature up to $U_f = 430$ W·m^{-2}K^{-1} at the highest operating temperature. Figures 10 and 11 present results comparing measured and modelled forward mode performances at varying condenser temperature and plate-to-plate temperature difference set-points, including several repeat tests to check repeatability. Measured thermal conductances varied from $U_f = 150$ to 500 W·m^{-2}K^{-1}. These have been compared to corresponding values predicted by the theoretical model which was implemented as a Microsoft Excel spreadsheet with supporting Visual Basic macros and lookup tables to evaluate working fluid thermodynamic properties based on REFPROP software outputs.

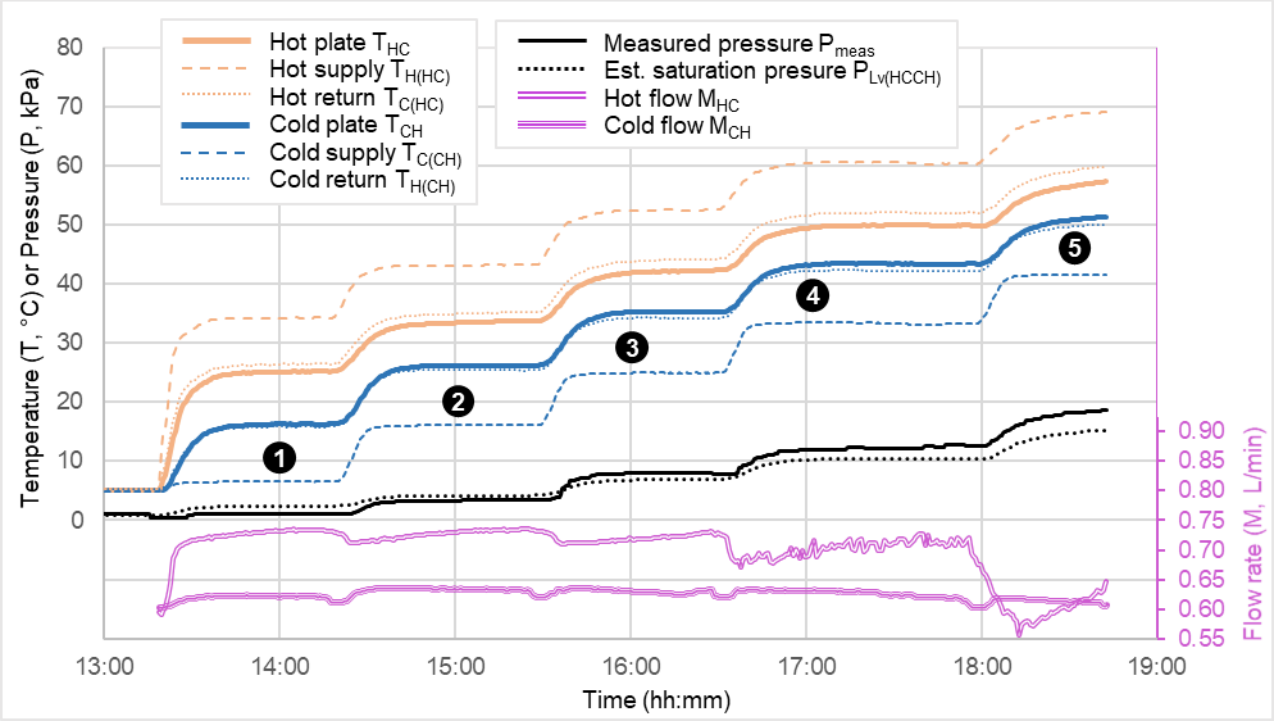

Figure 8 – Time history of measured temperatures, pressures & flows during forward mode tests with 11mm nylon spacer

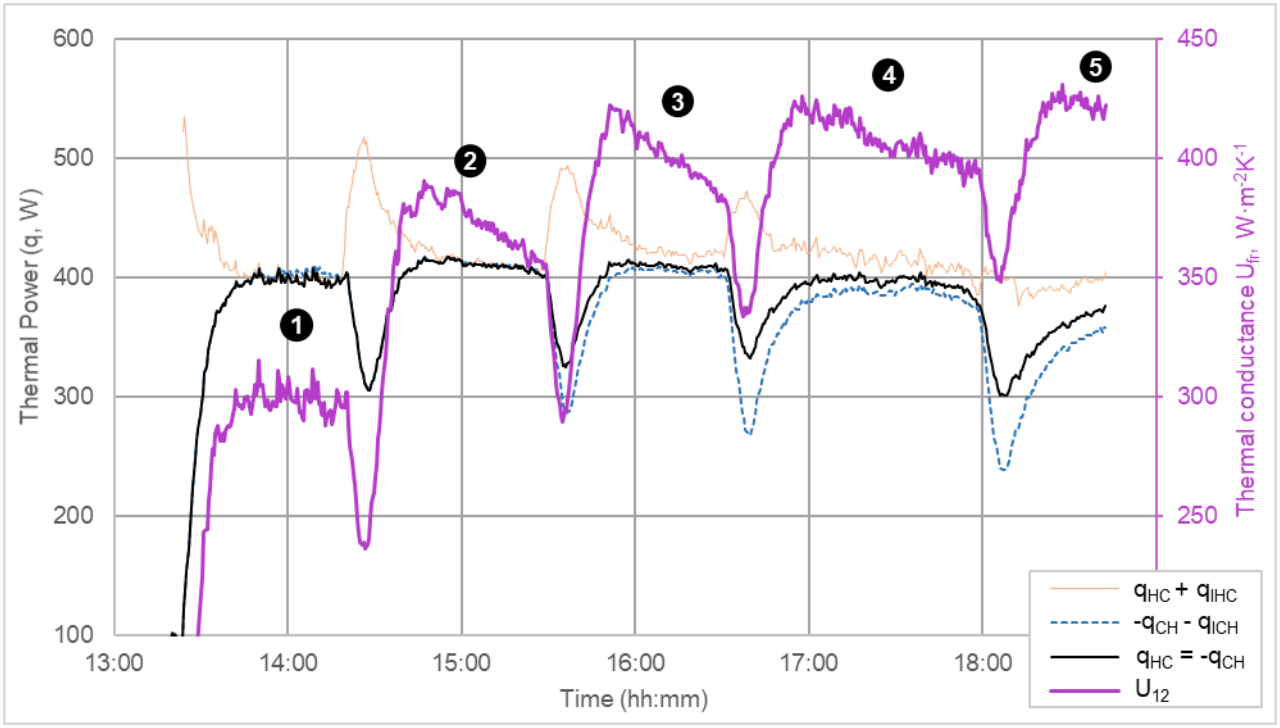

475
476 ***Figure 9 – Time history of derived thermal powers and conductance during forward mode tests with 11mm nylon spacer***
477
478

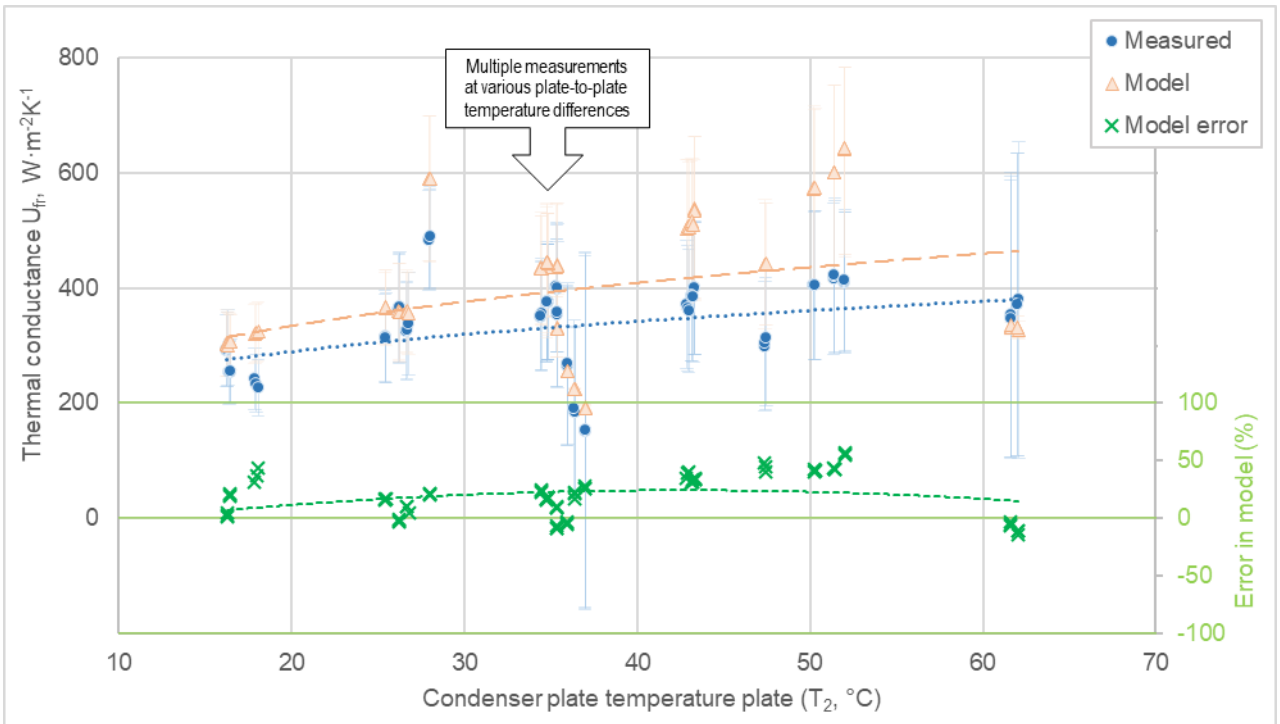

479
480 ***Figure 10 – Forward mode performance of PLVTD with 11 mm nylon spacer (varying condenser plate temperature)***
481
482
483

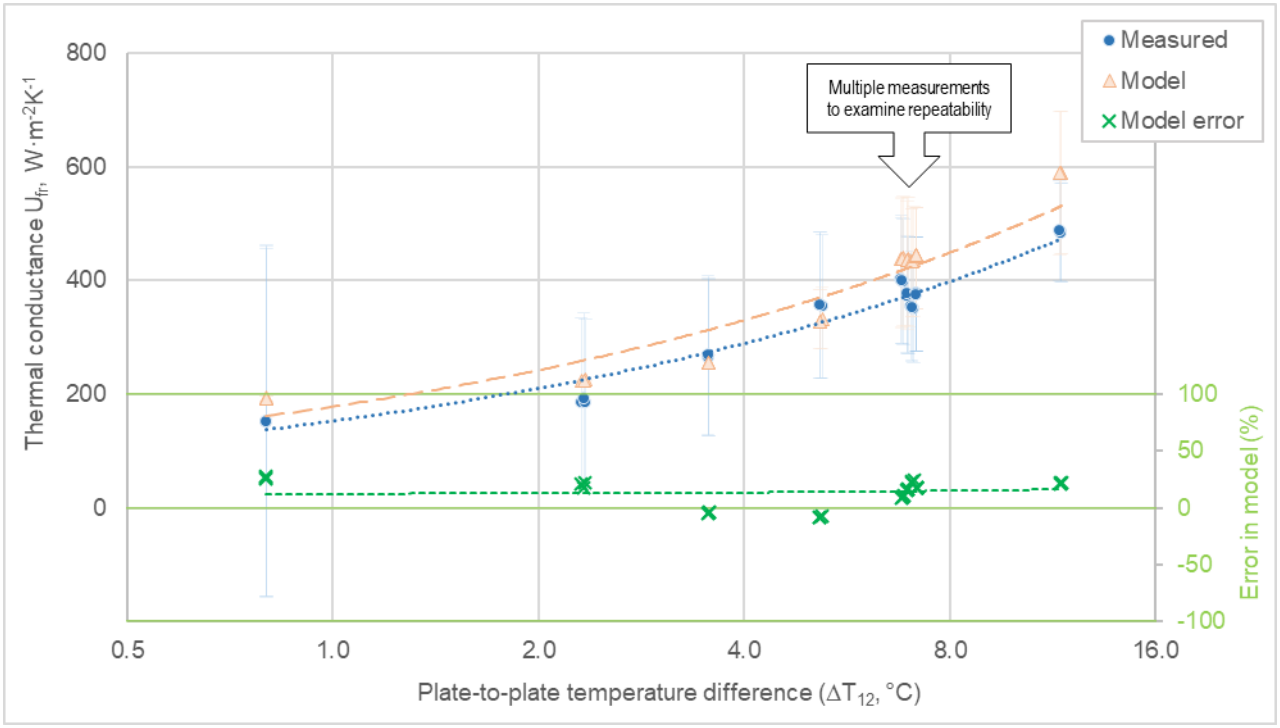

Figure 11 – Forward mode performance of PLVTD with 11 mm nylon spacer (varying plate-to-plate temperature difference)

The measurement and modelling results show clearly that forward mode thermal conductance increases with increasing condenser temperature (T_2) and with increasing plate-to-plate temperature difference (ΔT_{12}). Detailed examination of the model suggests that this is primarily due to decreases in evaporation thermal resistance (R_e) and vapour mass flow resistance (R_{ec}) caused by reductions in working fluid viscosity as temperature increases and by increased driving forces as plate-to-plate temperature differences (and hence saturation pressure differences) increase.

Error bars on the graphs indicate estimated combined measurement uncertainties (95% confidence limits) which are primarily associated with temperature and temperature difference measurement uncertainties. Results for cases where plate-to-plate temperature differences exceed ΔT_{12}>4°C have measurement uncertainties of less than ±40% but uncertainty increases at lower plate-to-plate temperature differences. Uncertainties propagate into the modelled results because measured plate temperatures are used as a calculation input parameter. Notwithstanding the declared measurement uncertainties (which have been estimated using a very conservative approach) it is clear that the model predicts the measured forward mode heat transfer behaviour reasonably well. An inherent bias is apparent in the data causing the model to consistently overpredict the heat transfer coefficients by +20% relative to the measured data. There are a number of possible reasons for this bias but the most likely explanation is the presence of non-condensable gasses (air) in the PLVTD which

increases thermal resistances associated with vapour mass transfer (R_{ec}) and condensation (R_c) as described by Stein et al. (1985) and Peterson (1996). This explanation is consistent with the fact that measured pressures (P_{meas}) were in some cases up to 25% higher than the estimated saturation pressures ($P_{Lv(HCCH)}$) as apparent in results towards the right of Figure 8.

Figures 12 and 13 present results comparing measured and modelled reverse mode performances at varying condenser plate temperatures and varying plate-to-plate temperature difference set-points. The measured thermal conductance was consistently around U_r=10 W·m^{-2}K^{-1} as predicted by the model and largely unaffected by varying plate temperatures or temperature differences. Detailed examination of the model suggests that conduction through PLVTD side walls (the 11mm nylon spacer frame, vacuum seals, and perimeter bolts) is the dominant heat transfer path amounting to U_w=6.7 W·m^{-2}K^{-1}. Gaseous conduction through water vapour in the cavity amounts to U_v=1.8 W·m^{-2}K^{-1} and radiant heat transfer amounts to U_R=1.1 W·m^{-2}K^{-1}.

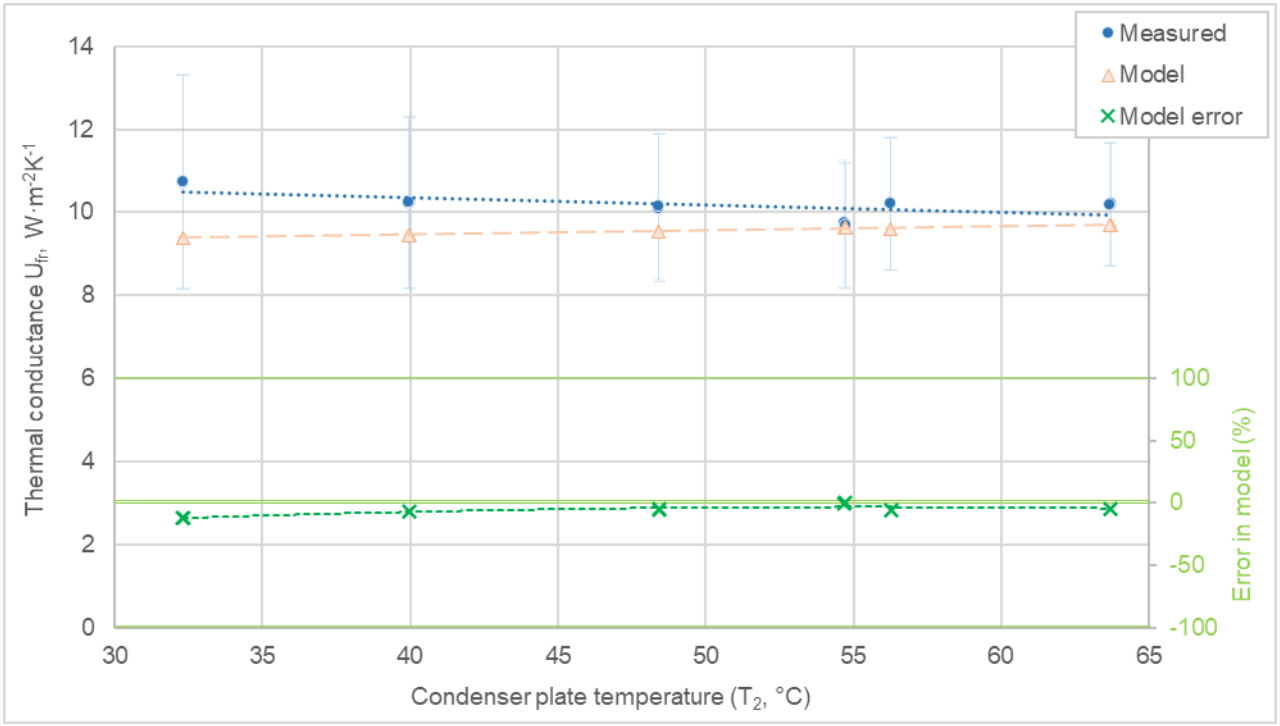

Figure 12 – Reverse mode performance of PLVTD with 11 mm nylon spacer (varying condenser plate temperature)

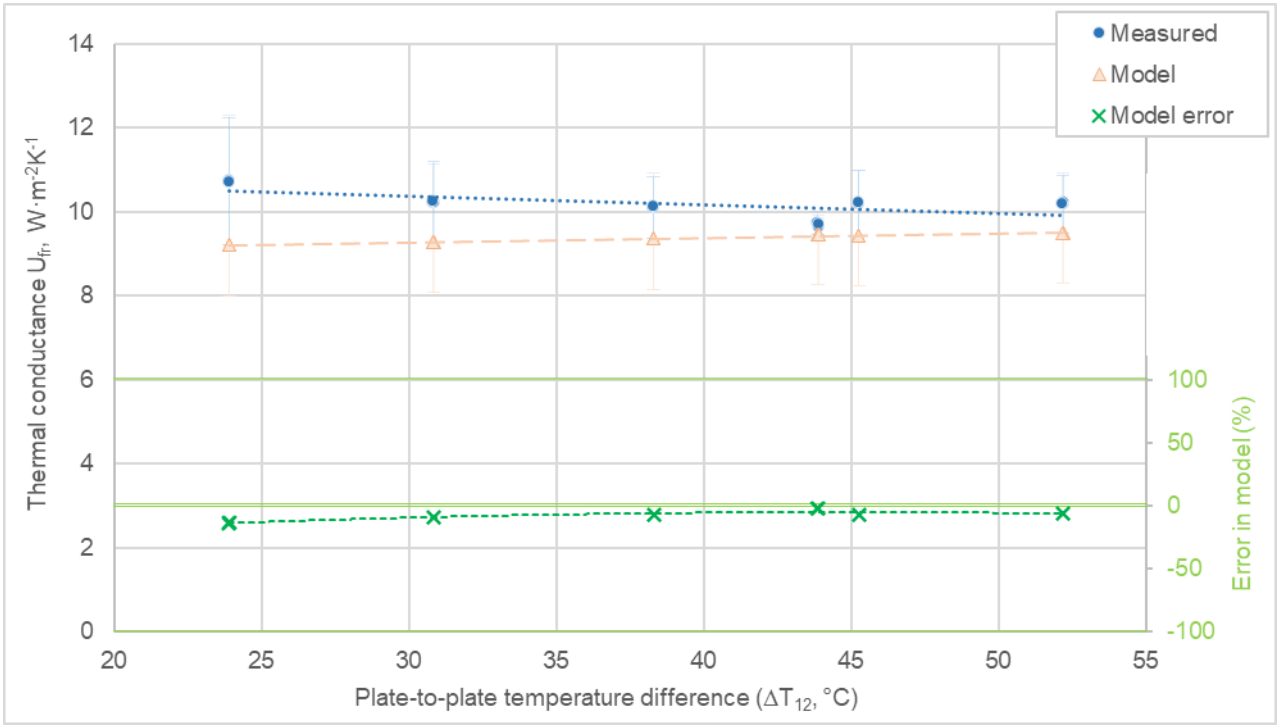

Figure 13 – Reverse mode performance of PLVTD with 11 mm nylon spacer (varying plate-to-plate temperature difference)

6 Discussion

The measurement results provide a reasonable validation for the theoretical results despite significant uncertainty associated with measurements of inherently small plate-to-plate and inlet-outlet water circuit temperature differences. The forward mode heat transfer performances in the range $150<U_f<500$ $W \cdot m^{-2}K^{-1}$ combined with the reverse mode insulation of $U_r=10$ $W \cdot m^{-2}K^{-1}$ corresponds to diodicity of $\varsigma \approx 88\%$ at low condenser temperatures and low heat fluxes ($T_2 \approx 15°C$ and $q/A \approx 120$ $W \cdot m^{-2}$) and $\varsigma \approx 96\%$ at high condenser temperatures and high heat fluxes ($T_2 \approx 60°C$ and $q/A \approx 2800$ $W \cdot m^{-2}$). Forward mode performance increases with increasing heat flux and (to a lesser extent) with increasing operating temperature. Reverse mode performance is largely independent of heat flux and temperature within the ranges investigated.

Comparing with the work of Boreyko & Chen (2011 & 2013) and Traipattanakul et al. (2019) suggests that the PLVTD examined in this study achieves similar or lower reverse mode (better thermal insulation) performances but somewhat lower forward mode (worse heat transfer) performances. The theoretical model indicates that the reverse mode performance is largely governed by cavity depth and the influence of thermal bridging elements (sidewalls and supporting structure) hence the findings are unsurprising given that cavity depths are of broadly similar magnitudes. The lower forward mode performance achieved in the present study is partly attributable to heat

548 flux (authors cited above examined behavior at higher heat fluxes) but more
549 importantly due to the simple design of the evaporator and condenser (authors cited
550 above used hydrophobic condenser coatings and hydrophilic evaporator wick coatings
551 to boost performance). Compared to the simple thermosyphonic thermal diode
552 investigated by Wong et al. (2019) the evacuated PLVTD examined in this study
553 achieves better performance in both forward and reverse modes, despite having a
554 smaller cavity depth. Evacuation reduces natural convection in reverse mode due to
555 removal of non-condensable gases and increases latent heat transfer in forward mode
556 because the cavity pressure is similar to the working fluid saturation pressure.

557 A key consideration for solar collector and climate control building envelope
558 applications is the thermal insulation performance (reverse mode) which typically
559 needs to be in the range offered by conventional insulation materials. For reference,
560 high quality double glazing typically achieves $U \approx 1.2$ $W \cdot m^{-2}K^{-1}$ and fibre or foam-based
561 insulation products (assuming 50mm thick) achieve $U \approx 0.7$ $W \cdot m^{-2}K^{-1}$. These values are
562 considerably lower (better) than those achieved by the PLVTD examined in this study
563 or by most other authors. Heat transfer performance of around 1000 $W \cdot m^{-2}K^{-1}$ is a
564 reasonable target for PLVTD forward mode performance when integrated in solar
565 thermal collectors (Dupeyrat et al., 2011). Analysis suggests that the overall collection
566 efficiency of a solar water heater would not be significantly affected by a 5-fold increase
567 or decrease to this target (Pugsley, 2017).

568 Using the theoretical model it is possible to examine a variety of PLVTD design options
569 in order optimise performance for solar collector and climate control building envelope
570 applications. Figure 14 shows how reverse mode performance (U_v) via natural
571 convection of water vapour is dependent upon the cavity depth ($L \approx x$) for nominal
572 assumed operating conditions (T_1=10°C and T_2=60°C). Calculations consider plate-to-
573 plate cavity depths in the range $10 \leq x \leq 200$ mm. It is very clear that increasing the
574 cavity depth improves the insulation performance. Figures 15 and 16 show the
575 calculated variation of reverse and forward mode performances with temperature for
576 a PLVTD of dimensions x=70mm, y=0.7m and z=1.4m constructed of x_p=z_w=1mm
577 thick stainless plates and sidewalls with internal supporting structure formed of
578 stainless steel tubular struts (d_s=8mm diameter and d_{sw}=1mm wall thickness) spaced
579 at d_{ss}=2_{dsxy}=2_{dsxz}=0.07m centres. The results demonstrate that such a design should
580 be capable of achieving insulation performances which are close to those desired and
581 diodicity ς>97%. It is interesting to note that the performances shown on Figures 15
582 and 16 are very similar to those shown on Figures 10 and 11, highlighting that forward
583 mode performance of a horizontal PLVTD is largely independent of dimensions.

Figure 17 shows that forward mode heat transfer is linearly dependent upon the plate-to-plate temperature difference below ΔT_{12}=3°C but follows an exponential relationship at higher plate temperature differences. The knee point corresponds to heat fluxes >1500 $W \cdot m^{-2}$ which may be of relevance to concentrating solar applications.

Pugsley (2016) constructed and tested a hybrid photovoltaic thermal integrated collector-storage solar water heater incorporating a PLVTD which had dimensions similar to those examined in Figures 15 to 17. The PLVTD achieved reverse mode performance of U_r=1.7 $W \cdot m^{-2}K^{-1}$ which enabled a satisfactory overall loss coefficient (U_{sys} = 0.85 $W \cdot m^{-2}K^{-1}$) to be achieved when the solar absorber was fitted with a rudimentary transparent plastic cover. The forward mode performance (U_f=45 $W \cdot m^{-2}K^{-1}$, similar to that achieved by Wong et al., 2019) was lower than expected owing to problems with dry patches on the evaporator surface. Overall diodicity (ς=93%) was marginally lower than expected.

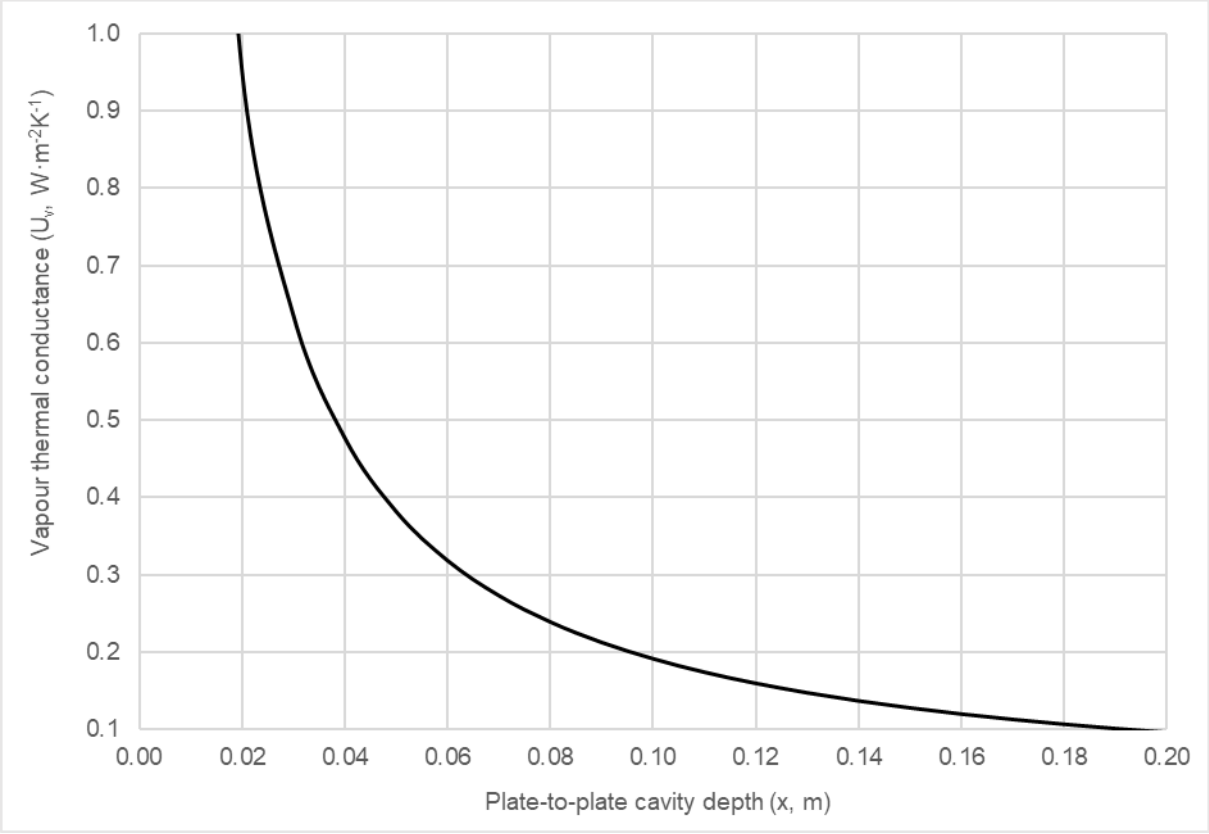

Figure 14 – Dependence of reverse mode water vapour thermal conductance on cavity depth in a horizontal PLVTD

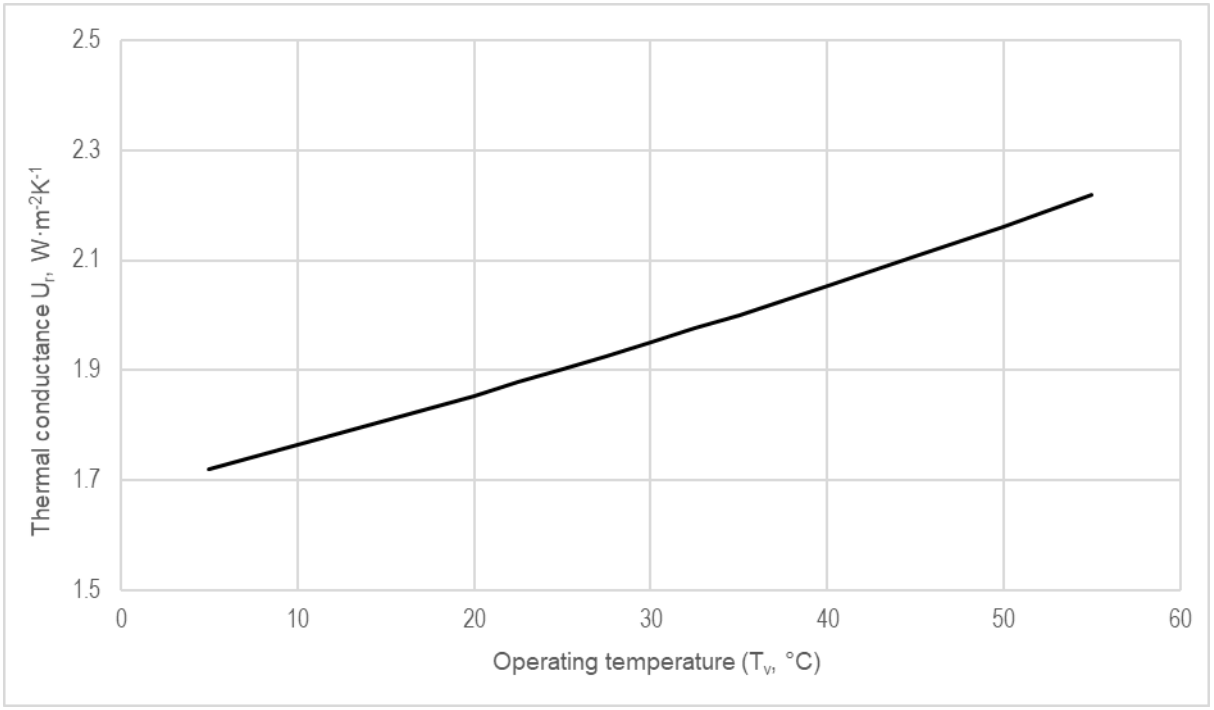

602
603 ***Figure 15 – Reverse mode temperature dependence (ΔT_{12} = 50°C) for a horizontal x = 0.07, y = 0.7, z = 1.4m stainless steel PLVTD***
604

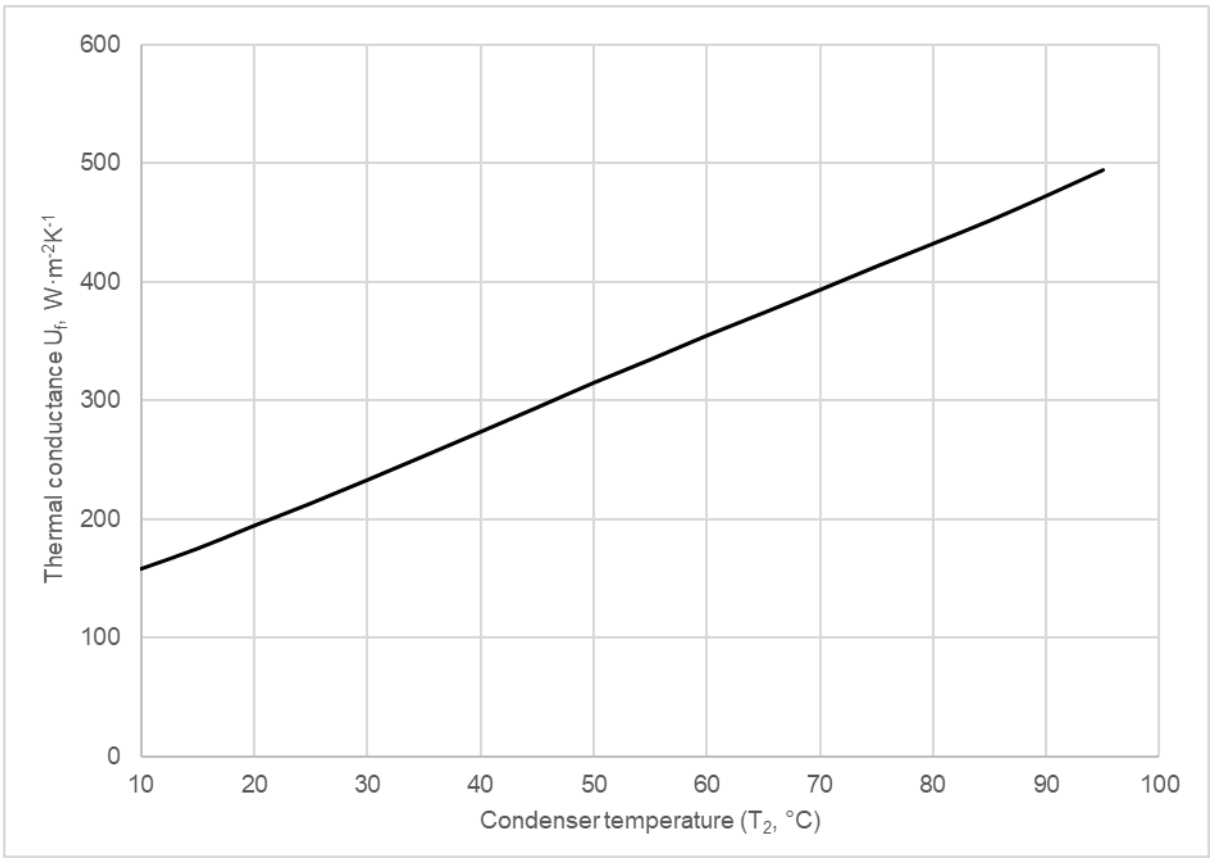

605
606 ***Figure 16 – Forward mode temperature dependence (ΔT_{12} = 1.5°C) for a horizontal x = 0.07, y = 0.7, z = 1.4m stainless steel PLVTD***
607
608

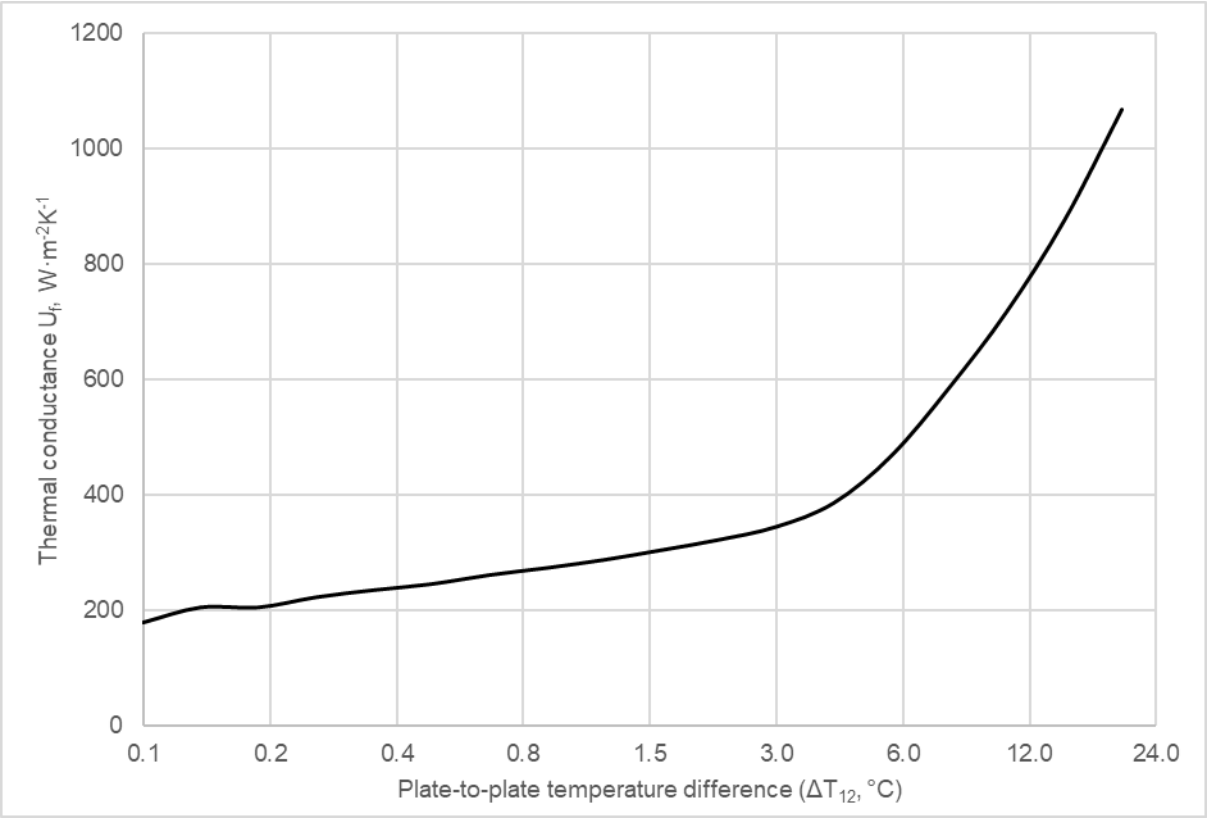

Figure 17 – Forward mode heat-flux dependence (T_2 = 45°C) for a horizontal x = 0.07, y = 0.7, z = 1.4m stainless steel PLVTD

7 Conclusions

The heat transfer behaviour of a horizontal planar liquid-vapour thermal diode (PLVTD) has been examined with the aim of supporting engineering for applications in solar thermal collectors and climate control building envelopes. An experimental PLVTD was fabricated and its forward mode heat transfer and reverse mode thermal insulation characteristics were quantified. The experimental device (A_p=0.15m^2 and x=11mm) examined in this study had a much larger area and wider cavity than PLVTDs reported elsewhere in the literature (A_p<0.01m^2 and 1<x<7mm). The experimental work involved a horizontally oriented PLVTD formed of two parallel isothermal plates with integral serpentine heat exchangers and external insulation. Temperature difference between the plates was controlled by connecting each serpentine heat exchanger to a separate heating-cooling fluid circuit. Plate, fluid, and ambient temperatures were measured to determine heat transfer coefficients under various temperature difference and heat flux operating scenarios. Forward mode heat transfer performances were found to be in the range 150<U_f<500 $W \cdot m^{-2}K^{-1}$ and reverse mode insulation was U_r=10 $W \cdot m^{-2}K^{-1}$. Forward mode performance was found to increase with increasing heat flux (in the range 120<q/A_p<2800 $W \cdot m^{-2}$) and to a lesser extent with increasing operating temperature (condenser plate temperatures in the range 15<T_2<60°C). Reverse mode

630 performance appears to be largely independent of heat flux and temperature within
631 the ranges investigated. The measured results correspond to diodicity in the range
632 $88<\varsigma<96\%$.

633 A one-dimensional lumped parameter heat transfer model has been proposed and
634 successfully validated using the experimental results. Examination of the model shows
635 that behaviour in forward mode is largely governed by the evaporation thermal
636 resistance (R_e) and vapour mass flow resistance (R_{ec}) which are sensitive to working
637 fluid viscosity and plate-to-plate temperature differences. The experimental work was
638 undertaken with non-condensable gases removed as far as possible, although a degree
639 of outgassing appears to have taken place during measurements. The vapour mass
640 flow resistance (R_{ec}) and the condensation thermal resistance (R_c) are sensitive to non-
641 condensable gases resulting the model generally overestimating the measured forward
642 mode performance by about 20%. Reverse mode performance is largely governed by
643 cavity depth which determines the thermal resistance of the sidewalls (R_w), the
644 supporting structural elements (R_s), and the gaseous conduction and convection across
645 the cavity (R_v). The radiative resistance between the two plates (R_r) had only a small
646 effect on the overall behavior of the device tested.

647 Whilst maximisation of forward mode heat transfer has been a priority for researchers
648 examining PLVTDs for electronics cooling applications, minimisation of reverse mode
649 heat transfer (ie improving the insulation performance) is the primary focus for PLVTDs
650 in solar collector and climate control building envelope applications. The theoretical
651 model has been used to calculate the forward and reverse mode performance of a
652 large area ($A_p=1m^2$) wide cavity (x=70mm) PLVTD constructed of 1mm stainless plates
653 and sidewalls with internal supporting structure formed of stainless-steel tubular struts
654 spaces at 70mm centres. The results demonstrate that such a design should be capable
655 of achieving forward mode heat transfer of $150<U_f<500$ $W\cdot m^{-2}K^{-1}$, reverse mode heat
656 transfer of $U_r=2$ $W\cdot m^{-2}K^{-1}$ and diodicity of $\varsigma>97\%$, which would be suitable for solar
657 collector and climate control building envelope applications.

658 The work presented in this paper is limited to simple horizontally oriented PLVTDs
659 where evaporator wetting and condensate return is driven by gravity. The authors
660 have subsequently examined the behaviour of modified PLVTDs in vertical and tilted
661 orientations. Experimental results for vertically oriented PLVTDs together with a
662 modified version of the lumped parameter model (to account for orientation) will be
663 presented in a future publication.

8 Acknowledgements

This research was enabled in its early stages by studentship funding support from the Northern Ireland Department for the Economy. The work was subsequently progressed with funding support from SolaForm Ltd and was completed as part of the "SolaFin2Go" project funded by the UKRI Engineering and Physical Sciences Research Council (EP/R035954/1) and Innovate UK Energy Catalyst Round 5 (IUK/133219). The authors would also like to thank networking support funded by the European Union FP7 COST Action TU1205 "Building Integration of Solar Thermal Systems".

9 Nomenclature

Latin symbols

A	Surface area [m^2]
c_p	Specific heat capacity at constant pressure [$J \cdot kg^{-1} K^{-1}$]
d	Distance [m]
g	Acceleration due to gravity (g=9.81$m \cdot s^{-2}$ on earth at sea level)
h_{Lv}	Latent heat of liquid-vapour phase change [$J \cdot kg^{-1}$]
k	Thermal conductivity [$W \cdot m^{-1} K^{-1}$]
L	Characteristic dimension of Nusselt number [m]
M	Mass flow rate [$kg \cdot s^{-1}$]
N	Number of struts in structural support array
Nu	Nusselt number
P	Pressure [Pa]
Pr	Prandtl number
q	Thermal power [W]
Ra	Rayleigh number
T	Temperature [°C] except for Equation 10 which uses absolute [K]
U	Thermal conductance or heat transfer coefficient [$W \cdot m^{-2} K^{-1}$]
v	Kinematic viscosity [$m^2 \cdot s^{-1}$]
x	Distance along an axis which is parallel to the PLVTD depth [m]
y	Distance along horizontal axis perpendicular to PLVTD depth [m]
z	Distance along an axis which is perpendicular to x and y axes [m]

Greek and other symbols

$\mathcal{M}$	Molecular weight [$g \cdot mol^{-1}$]
$\mathcal{R}$	Universal gas constant (8.314 $J \cdot mol^{-1} K^{-1}$)
ϑ	Thermal diffusivity [$m^2 \cdot s^{-1}$]

698	ΔP	Pressure difference [Pa]
699	ΔT	Temperature difference [°C]
700	ς	Diodicity [%]
701	σ	Surface tension [$N \cdot m^{-1}$]
702	β	Coefficient of volumetric expansion [K^{-1}]
703	ρ	Density [$kg \cdot m^{-3}$]
704	χ	Stefan Boltzmann constant (5.67×10^{-8} $W \cdot m^{-2}K^{-4}$)

705 ***Subscripts***

706	1	Plate 1 which is the evaporator in forward mode
707	2	Plate 2 which is the condenser on forward mode
708	12	Between (or average of) the two plates
709	a	Ambient environment
710	B	Back of plate
711	c	Condenser, condensate or condensation
712	C	Cold water feed or cooled return
713	CH	Cooling plate or cooling water circuit
714	D	Edge of plate
715	e	Evaporator, evaporation or evaporator liquid film
716	ec	Between (or average of) the evaporator and condenser surfaces
717	f	Forward mode
718	H	Hot water feed or heated return
719	HC	Heating plate of heated water circuit
720	L	Working fluid liquid state property
721	l	Losses to ambient environment
722	L1	Liquid on the evaporator
723	L2	Liquid on the condenser
724	Lv	Latent property of working fluid at the liquid-vapour saturation point
725	LvL	Liquid-vapour-liquid transition
726	p	Plate
727	r	Reverse mode
728	R	Radiative component
729	s	Structural element(s) such as internal support struts
730	ss	Between two adjacent struts (centre-to-centre distance)
731	sw	Strut tube wall (thickness)
732	sxy	Between the xy-sidewall and the closest strut (distance along the z-axis)

sxz	Between the xz-sidewall and the closest strut (distance along the y-axis)
v	Working fluid vapour state property
w	Sidewalls of the PLVTD
x	In the direction parallel to the PLVTD depth
y	In the direction of the horizontal axis perpendicular to PLVTD depth
z	In the direction of the axis which is perpendicular to x and y axes

10 References

Avanessian, T. & Hwang, G. (2018). Thermal diode using controlled capillary in heterogeneous nanopores. International Journal of Heat and Mass Transfer 124 (2018) 201–209

Baïri, A., Zarco-Pernia, E., García de María, J. (2014). A review on natural convection in enclosures for engineering applications. The particular case of the parallelogrammic diode cavity. Applied Thermal Engineering 63 (2014) 304-322

Ben-Abdallah, P and Biehs, S. (2013). Phase-change radiative thermal diode. Applied Physics Letters 103 (19)

Blet, N., Lips, S., Sartre, V. (2017). Heats pipes for temperature homogenization: A literature review. Applied Thermal Engineering 118 (2017) 490–509

Boreyko, J. & Chen, C. (2013). Vapor chambers with jumping-drop liquid return from superhydrophobic condensers. International Journal of Heat and Mass Transfer 61 (2013) 409–418

Boreyko, J., Zhao, Y., Chen, C. (2011). Planar jumping-drop thermal diodes. Applied Physics Letters 99, 234105

Chen, K., Chailapo, P., Chun, W., Kim, S., Lee, K. (1998). The Dynamic Thermosiphon of a bayonet-type thermal diode. Solar Energy 64 (4–6) 257–263

Chen (2012). Patent Application for Thermal Diode Device and Methods. US 2012/0012804 Al

Collins, R. & Fischer-Cripps, A. (1991). Design of Support Pillar Arrays in Flat Evacuated Windows. Australian Journal of Physics 1991 (44) 545-63

De Beijer, H. (1998). Product development in solar water heating. Renewable Energy 5 (1998) 201-204

Dos Santos Bernardes, M. (2014). Experimental evidence of the working principle of thermal diodes based on thermal stress and thermal contact conductance – Thermal semiconductors. International Journal of Heat and Mass Transfer 73 (2014) 354–357

Dupeyrat, P., Menezo, C., Rommel, M., Henning, H. (2011). Efficient single glazed flat plate photovoltaic-thermal hybrid collector for domestic hot water systems. Solar Energy 85, 1457-68

Fang, Y., Hyde, T., Arya, F., Hewitt, N., Eames, P., Norton, B., Miller, S. (2014). Indium alloy-sealed vacuum glazing development and context. Renewable and Sustainable Energy Reviews 37 (2014) 480–501

Gaddam, P., Huxtable, S., Ducker, W. (2017). A liquid-state thermal diode. International Journal of Heat and Mass Transfer 106 (2017) 741–744

Gerstmann, J. & Griffith, P. (1967). Laminar Film Condensation on the Underside of Horizontal and Inclined Surfaces. International Journal of Heat and Mass Transfer 10 (1967) 567-80.

Go, D. & Sen, M. (2010). Thermal Rectification Using Bulk Materials. ASME Journal of Heat Transfer 132 (12) 124502

Hess, T., Maier, L., Corhan, P., Schäfer–Welsen, O., Wöllenstein, J., Bartholomé, K. (2019). Modelling cascaded caloric refrigeration systems that are based on thermal diodes or switches. International Journal of Refrigeration 103 (2019) 215–222

Muhumuza, R., Zacharopoulos, A., Mondol, J., Smyth, M. (2019a). Experimental study of heat retention performance of thermal diode Integrated Collector Storage Solar Water Heater (ICSSWH) configurations. Sustainable Energy Technologies and Assessments 34 (2019) 214–219

Muhumuza, R., Zacharopoulos, A., Mondol, J., Smyth, M., Pugsley, A., Giuzio, G., Kurmis, D. (2019b). Experimental investigation of horizontally operating thermal diode solar water heaters with differing absorber materials under simulated conditions. Renewable Energy, Volume 138, August 2019, Pages 1051-1064

NIST (2013). Standard Reference Database 23 Version 1. Gaithersburg, MD, USA: National Institute of Standards and Technology (NIST) US Department of Commerce. (Accessed via REFPROP software).

Pan, Y., Wu, C. Z. (2002). Numerical investigations and engineering applications on freezing expansion of soil restrained two-phase closed thermosyphons. International Journal of Thermal Sciences 41 (2002) 341–347

Pei, W., Zhang, M., Li, S., Lai, Y., Jin, L., Zhai, W., Yu, F., Lu, J. (2017). Geotemperature control performance of two-phase closed thermosyphons in the shady and sunny slopes of an embankment in a permafrost region. Applied Thermal Engineering 112 (2017) 986–998

Peterson, P. (1996). Theoretical basis for the Uchida correlation for condensation in reactor containments. Nuclear Engineering and Design 162 (1996) 301-306.

Pugsley, A., Mondol, J., Smyth, M., Zacharopoulos, A. & Di Mattia, L. (2016). Experimental characterisation of a flat panel integrated collector-storage solar water heater featuring a photovoltaic absorber and a planar liquid-vapour thermal diode. Proceedings of 11th ISES EuroSun Conference: Palma (Mallorca), Spain from 11 to 14 October 2016. Martinez, V. & Gonzalez, J. (eds.).

802 Pugsley, A. (2017). Theoretical and experimental analysis of a novel flat photovoltaic-thermal
803 solar water heater with integrated energy storage via a planar liquid-vapour thermal diode.
804 Ulster University PhD Thesis (uk.bl.ethos.713462) published July 2017.

805 Quinlan, P. (2010). The Development of a Novel Integrated Collector Storage Solar Water
806 Heater (ICSSWH) Using Phase Change Materials and Partial Evacuation. PhD Thesis, University
807 of Ulster.

808 Reay, D., Kew, P., McGlen, R. (2014). Heat Pipes - Theory, Design and Applications (6th
809 edition). London, UK: Butterworth-Heinemann (Elsevier). ISBN: 0080982794

810 Roberts, N. & Walker, D. (2011). A review of thermal rectification observations and models in
811 solid materials. International Journal of Thermal Sciences 50 (2011) 648-62.

812 Shen, J., Liu, X., He, H., Wu, W., Liu, B. (2018). High-performance noncontact thermal diode
813 via asymmetric nanostructures. Journal of Quantitative Spectroscopy & Radiative Transfer
814 211 (2018) 1–8

815 Smyth, M. (2015a). A solar water heater. Patent WO2010052010 held by Ulster University.

816 Smyth, M., Besheer, A., Zacharopoulos, A., Mondol, J., Pugsley, A., Novaes, M. (2015b).
817 Experimental evaluation of a Hybrid Photovoltaic/Solar Thermal (HyPV/T) Façade Module.
818 Proceedings EURO ELECS Conference 21-23 July 2015, Guimarães, Portugal.

819 Smyth, M., Quinlan, P., Mondol, J., Zacharopoulos, A., McLarnon, D., Pugsley, A. (2017). The
820 evolutionary thermal performance & development of a novel thermal diode pre-heat solar water
821 heater under simulated heat flux conditions. Renewable Energy 113 (2017) 1160-1167

822 Smyth, M., Quinlan, P., Mondol, J., Zacharopoulos, A., McLarnon, D., Pugsley, A. (2018). The
823 experimental evaluation and improvements of a novel thermal diode pre-heat solar water
824 heater under simulated solar conditions. Renewable Energy 121 (2018) 116-122

825 Smyth, M., Pugsley, A., Hanna, G., Zacharopoulos, A., Besheer, A., Savvides, A. (2019).
826 Experimental performance characterisation of a Hybrid Photovoltaic/Solar Thermal Façade
827 module compared to a flat Integrated Collector Storage Solar Water Heater module. Renewable
828 Energy 137 (2019) 137-143

829 Souliotis, M., Quinlan, P., Smyth, M., Tripanagnostopoulos, Y., Zacharopoulos, A., Ramirez, M.,
830 Yianoulis, P. (2011). Heat retaining integrated collector storage solar water heater with
831 asymmetric CPC reflector. Solar Energy 85 (2011) 2474–87

832 Souliotis, M., Papaefthimiou, S., Caouris, Y., Zacharopoulos, A., Quinlan, P., Smyth, M. (2017).
833 Integrated collector storage solar water heater under partial vacuum. Energy 139 (2017) 991-
834 1002

835 Stein, R., Cho, D., Lambert, G. (1985). Condensation on the underside of a horizontal surface
836 in a closed vessel (CONF-850810-27). Argonne, Illinois, USA: Argonne National Laboratory.
837 Available at: www.osti.gov/scitech/biblio/5207060

838 Traipattanakul, B., Tso, C., Chao, C. (2019). A phase-change thermal diode using electrostatic-
839 induced coalescing jumping droplets. International Journal of Heat and Mass Transfer 135
840 (2019) 294–304

841 Tso, C., Chao, C. (2016). Solid-state thermal diode with shape memory alloys. International
842 Journal of Heat and Mass Transfer 93 (2016) 605–611

843 Twidell, J. & Weir, T. (2006). Renewable Energy Resources (2nd ed.) London: Taylor Francis.
844 ISBN13:9-78-0-419-25330-3

845 Varga, S., Oliveira, A., Afonso, C. (2002). Characterisation of thermal diode panels for use in
846 the cooling season in buildings. Energy and Buildings 34 (2002) 227-235

847 Villeneuve, T., Boudreau, M., Dumas, G. (2017). The thermal diode and insulating potentials of
848 a vertical stack of parallelogrammic air-filled enclosures. International Journal of Heat and Mass
849 Transfer 108 (2017) 2060–2071

850 Wong, M., Traipattanakul, B., Tso, C., Chao, C., Qiu, H. (2019). Experimental and theoretical
851 study of a water-vapor chamber thermal diode. International Journal of Heat and Mass Transfer
852 138 (2019) 173–183